Understanding the Role of Biogenic Magnetite in Geomagnetic Paleointensity Recording: Insights from Ontong Java Plateau Sediments

Jiaxi Li[1], Toshitsugu Yamazaki[1], Yoichi Usui[2], Takuya Sagawa[3], Yoshimi Kubota[4], and Junichiro Kuroda[1]

[1]Atmosphere and Ocean Research Institute, The University of Tokyo, Kashiwa, Japan

[2]Volcanoes and Earth's Interior Research Center, Research Institute for Marine Geodynamics, Japan Agency for Marine-Earth Science and Technology, Yokosuka, Japan

[3]Institute of Science and Engineering, Kanazawa University, Kanazawa, Japan

[4]Department of Geology and Paleontology, National Museum of Nature and Science, Tsukuba, Japan

Corresponding author: Jiaxi Li (li-jiaxi316@g.ecc.u-tokyo.ac.jp)

Key Points:

- ARM-normalized relative paleointensity is inversely correlated with the proportion of biogenic magnetite in the studied sediments.
- The estimated relative paleointensity recording efficiency of biogenic magnetite is lower than that of terrigenous magnetic minerals.
- Different concentrations of silicate-hosted magnetic inclusions might cause our results to be contrary to those of previous studies.

Abstract

Marine sediments can preserve continuous paleomagnetic intensity records. Because different magnetic minerals may acquire remanent magnetizations differently, compositional variations of magnetic mineral assemblages in sediments may hinder extraction of reliable relative paleointensity (RPI) records. To better understand this issue, we conducted a paleo- and rock magnetic study of a sediment core from the Ontong Java Plateau in the western equatorial Pacific Ocean. RPI estimated by normalizing natural remanent magnetization with anhysteretic remanent magnetization (ARM) decreases downcore with an inverse correlation with the ratio of ARM susceptibility to saturation isothermal remanent magnetization. This relationship indicates that the RPI signal weakens as the proportion of biogenic magnetite increases. The NRM–ARM demagnetization diagrams we compiled show concave-down curvature. These observations indicate that the RPI recording efficiency of the biogenic component is lower than that of the terrigenous component when we assume that the magnetizations of the high- and low-coercivity windows are carried dominantly by biogenic and terrigenous components, respectively. This assumption is supported by first-order reversal curve measurements, transmission electron microscope observations, low-temperature measurements, and extraction of silicate-hosted magnetic inclusions from the sediments. Previous studies have suggested that the RPI recording efficiency of biogenic magnetite is higher than that of the terrigenous component, which disagrees with our results. Different concentrations of silicate-hosted magnetic inclusions in different sedimentary environments might explain this contradiction. We concluded that biogenic magnetite contributes to RPI records with lower efficiency than unprotected terrigenous magnetic minerals in the studied sediments. Changing biogenic magnetite proportion distorts ARM-normalized RPI.

Plain Language Summary

Magnetic minerals in marine sediments can preserve the variations over geologic time of the intensity of Earth's magnetic field (paleointensity), which is important information for understanding how the field is generated within Earth's core. Paleointensity can be recorded by magnetic minerals with different recording efficiencies, so it can be difficult to recover reliable paleointensity records from sediments composed of different magnetic minerals. Our study of a sediment core from the western equatorial Pacific Ocean shows that paleointensity in the core is recorded by two main types of magnetic minerals: biogenic magnetite produced by bacteria that

align themselves with the Earth's magnetic field, and magnetic minerals produced by weathering of terrigenous sediments. The paleointensity record we obtained from the sediment core weakens with increasing abundance of biogenic magnetite in the sediments. We concluded that biogenic magnetite records paleomagnetic intensity less efficiently than terrigenous magnetic minerals, which conflicts with the results of previous studies. This contradiction might be explained by differences in the concentrations of magnetic minerals embedded in non-magnetic silicate minerals in our study area compared to those in the areas of the previous studies.

1. Introduction

The geomagnetic field is generated by a self-exciting magnetohydrodynamic system in Earth's core. Systematic analysis of geomagnetic field behavior requires not only directional information but also intensity variations. Studies of relative paleointensity (RPI) provide information about the past behavior of the geomagnetic field and contribute to our understanding of the inner workings of the Earth (Tauxe & Yamazaki, 2015). Moreover, changes of RPI recorded in marine sediments provide reference signals for sediment dating that are independent of conventional marine paleoceanographic proxies, such as the foraminiferal oxygen isotope ratios ($\delta^{18}O$).

Marine sediments can preserve continuous RPI records. In paleomagnetic studies of marine sediments, an approximately linear relation between the ambient geomagnetic field and the depositional remanent magnetization (DRM) intensity is assumed; however, we lack a solid theoretical foundation for the processes by which marine sediments acquire DRM. Although there has been considerable effort to understand DRM acquisition mechanisms (Mitra & Tauxe, 2009; Nagata, 1961; Tauxe et al., 2006), credible extraction of absolute geomagnetic field magnitudes from marine sediments has not yet been achieved. Moreover, the complexity of the composition of marine sediments and their multiple magnetic components can affect the natural remanent magnetization (NRM) preserved in marine sediments (i.e., DRM). Post-depositional processes, including sediment compaction and reductive diagenetic alteration, can also affect NRM (Roberts et al., 2013; Tauxe & Yamazaki, 2015).

An empirical approach for RPI estimations is to use artificial laboratory-induced magnetization to normalize NRM intensity, thus compensating for magnetic mineral concentration variations (Johnson et al., 1948; Levi & Banerjee, 1976). Homogeneity in magnetic mineralogy

and a narrow range of magnetic grain size are assessed with magnetic hysteresis and bulk rock magnetic parameters to limit non-geomagnetic factors that complicate extraction of RPI signals (Ouyang et al., 2014; Roberts et al., 2013; Tauxe, 1993). However, bulk magnetic properties often fail to identify complexly mixed magnetic-mineral assemblages with different origins and changing proportions, which could influence RPI estimation reliability. Terrigenous magnetic minerals have been recognized as paleointensity signal recorders in RPI investigations for decades. Recently, biogenic magnetite and silicate-hosted magnetic inclusions have also been recognized as stable, single-domain (SD) carriers of NRM, and their roles in RPI recording have been studied extensively (Amor et al., 2022; Chang et al., 2021; Chang, Roberts, et al., 2016; Chen et al., 2017; Hong et al., 2019; Ouyang et al., 2014; Paterson et al., 2013; Roberts et al., 2012; Usui & Yamazaki, 2021).

Biogenic magnetite, which is biomineralized by magnetotactic bacteria (MTB) in marine and lacustrine environments, is commonly found as magnetofossils in sediments (Kirschvink, 1982; Roberts et al., 2012; Yamazaki & Ikehara, 2012). MTB produce magnetite (or greigite) crystals with well-controlled SD sizes and shapes (Kopp & Kirschvink, 2008). The common occurrence of biogenic magnetite in the magnetic-mineral assemblages of marine sediments and its contribution to RPI recording have been widely recognized, owing partly to improved techniques for decomposing mixed magnetic-mineral assemblages, for example, by using isothermal remanent magnetization (IRM) acquisition curves and first-order reversal curve (FORC) diagrams (Egli, 2021; Roberts et al., 2012; Yamazaki, 2008, 2009; Yamazaki & Ikehara, 2012).

Silicate-hosted magnetic-mineral inclusions are another candidate for preserving paleomagnetic signals in sediments (Chang et al., 2021; Chang, Roberts, et al., 2016; Zhang et al., 2018). Host silicate minerals can protect magnetic-mineral inclusions from iron- and sulfate-reducing diagenesis, and the inclusions commonly occur as fine particles. Thus, paleomagnetic signals can potentially be recorded and preserved by silicate-hosted magnetic-mineral inclusions, even in sediments subjected to reductive diagenesis. However, it has been reported that the NRM recording efficiency of magnetic inclusions is lower than that of unprotected terrigenous magnetic minerals, partly because the geomagnetic aligning torque on magnetic inclusions is counteracted by the hydrodynamic settling force on oversized non-magnetic host silicates (Chang, Roberts, et al., 2016; Chen et al., 2017; Hong et al., 2019). A recent redeposition experiment on silicate-hosted magnetic inclusions further supported this idea and revealed that non-linear field-dependent NRM

114 acquisition is likely attributable to the magnetic moment distributions of embedded magnetic
115 inclusions as well as the size and shape of the host-silicate minerals (Chang et al., 2021).

116 The ratio between the anhysteretic remanent magnetization (ARM) susceptibility (k_{ARM})
117 and saturation IRM (SIRM) (i.e., k_{ARM}/SIRM) is often considered to be a grain-size proxy for
118 magnetic minerals in sediments (Banerjee et al., 1981; King et al., 1982). The strength of
119 magnetostatic interactions among magnetic particles can affect this ratio because ARM acquisition
120 efficiency can be influenced significantly by those interactions (Cisowski, 1981; Sugiura, 1979).
121 Biogenic magnetite has little magnetostatic interactions because of its distinctive chain-like
122 alignment of magnetite particles, although the strength of interactions may increase in multi-
123 stranded and collapsed biogenic magnetosome chains (Amor et al., 2022). In contrast, terrigenous
124 magnetic minerals tend to have strong magnetostatic interactions because they are more likely to
125 form aggregations. Biogenic magnetosomes are mostly confined within a narrow SD range of grain
126 sizes, whereas those of terrigenous magnetic minerals span superparamagnetic (SP) to vortex
127 and/or multi-domain (MD) states. The presence of larger proportions of biogenic magnetite could
128 thus enhance ARM acquisition efficiency by the combined influence of differences in grain-size
129 distribution and the strength of magnetostatic interactions, consequently producing a higher
130 k_{ARM}/SIRM ratio. Therefore, the k_{ARM}/SIRM ratio can be a proxy for the abundance of biogenic
131 magnetite relative to terrigenous components in magnetic-mineral assemblages, particularly in
132 pelagic environments, where the grain-size variability of terrigenous magnetic minerals would be
133 small (Egli, 2004; Yamazaki, 2008, 2012; Yamazaki & Ikehara, 2012; Yamazaki & Shimono,
134 2013; Yamazaki & Solheid, 2011). A reported correlation between k_{ARM}/SIRM and RPI for some
135 sediments (Hofmann & Fabian, 2009; Sakuramoto et al., 2017; Yamazaki et al., 2013) may be a
136 universal problem whereby compositional variations of sediments affect the reliability of RPI
137 estimations. This problem needs to be understood and resolved.

138 In this study, we used a sediment core from the western equatorial Pacific Ocean to
139 investigate the influence of compositional variations in sediments on RPI estimations. Variable
140 relative proportions of biogenic and terrigenous components in sediments can have a considerable
141 influence on the RPI records in sediments (Inoue et al., 2021; Roberts et al., 2012; Yamazaki et
142 al., 2013). Some previous research has suggested that biogenic magnetite acquires RPI more
143 efficiently than terrigenous magnetite (Chen et al., 2017; Ouyang et al., 2014). In this study, we
144 sought to further understand how magnetic minerals derived from different sources contribute to

145 the remanent magnetization and RPI recording of sediments due to different proportions of
146 biogenic and terrigenous components.

147 ## 2. Study Materials and Age Model

148 The samples used in this study were taken from a piston core acquired from the Ontong
149 Java Plateau in the western equatorial Pacific Ocean (Figure 1). The 13.6-m-long piston core
150 MR1402-PC4 (2°03.00′N, 156°06.48′E; water depth 2447 m) consists of Quaternary sediments,
151 which was expected to provide a continuous Pleistocene geomagnetic record. The site lies above
152 the present carbonate compensation depth, which is at a water depth of about 5250 m in the study
153 area (Valencia, 1973). The predominant core sediment is light gray to light olive-gray calcareous
154 ooze. Foraminifera and calcareous nannofossils are the most abundant sediment constituents, and
155 clay minerals are also common. The sediments experienced a moderate to strong bioturbation
156 throughout the core. There is a clear sediment color change from brown to gray about 20 cm below
157 the sediment-water interface, which indicates the Fe-redox boundary (Yamazaki & Solheid, 2011).

158 The core was cut into 1-m-long sections and then split into working and archive halves
159 using a nylon line splitting device onboard R/V *Mirai*. Two rows of discrete samples (7 cm^3 each)
160 were taken continuously from the split-core surface in open-ended plastic cubes. One row was for
161 paleomagnetic and rock-magnetic measurements, the other for oxygen-isotope measurements.
162 Immediately after collection the samples were sealed tightly to prevent dehydration.

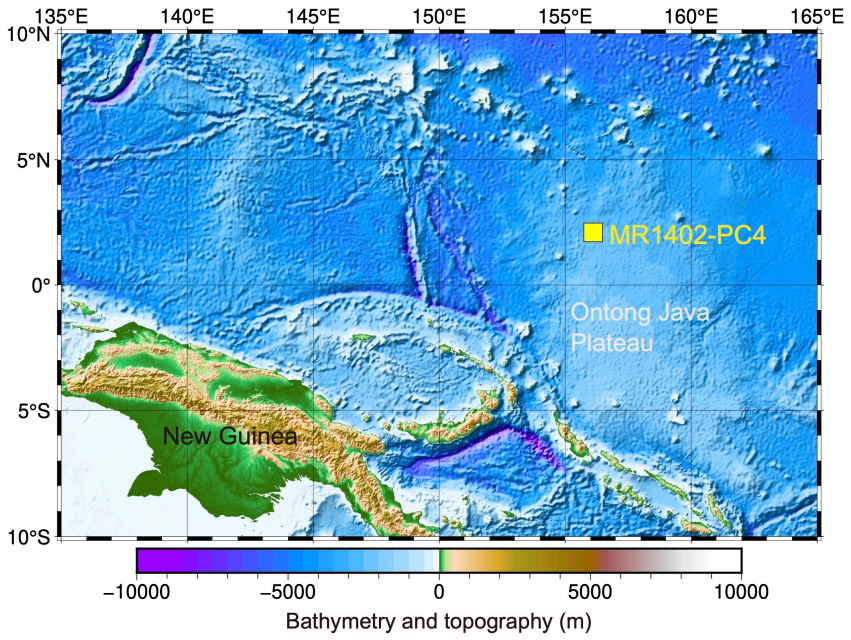

163

Figure 1. Location of core MR1402-PC4 in the western equatorial Pacific Ocean. Bathymetry and topography data were obtained from the ETOPO1 Global Relief Model developed by the National Oceanic and Atmospheric Administration.

An age model for core MR1402-PC4 was constructed using $\delta^{18}O$ stratigraphy (Figure 2). About 30 specimens of the planktonic foraminifera *Pulleniatina obliquiloculata* were picked from the 355–425 μm size fraction of every sample. The foraminiferal shells were gently crushed between two glass plates under the microscope to ensure that all chambers were open. The fragments were transferred to acid-cleaned 500 μL polypropylene microtubes. After ultrasonication with Milli-Q water and methanol, a small portion of the fragments was used for $\delta^{18}O$ analysis. Measurements were conducted with a ThermoFisher Scientific MAT253 mass spectrometer connected to a Kiel IV carbonate device at the National Museum of Nature and Science, Tsukuba, Japan. Isotope values were calibrated using the NBS-19 standard, which was analyzed several times in each run for every 7–8 unknown samples. The standard deviations for all samples were less than 0.06‰ (1σ). The $\delta^{18}O$ curve for *P. obliquiloculata* was visually fit to the LR04 benthic $\delta^{18}O$ stack (Lisiecki & Raymo, 2005) at 24 tie points (Figure 2). We estimated an average sedimentation rate of ~1.4 cm/kyr at the core location.

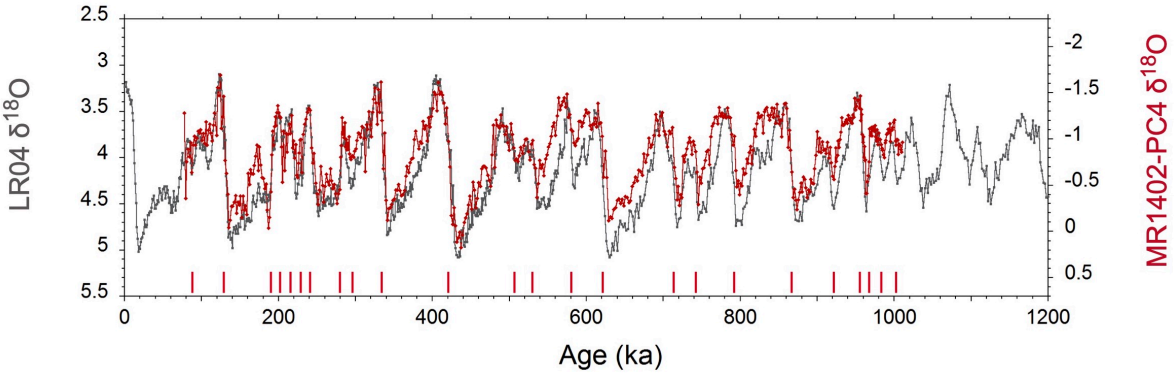

Figure 2. Measured $\delta^{18}O$ values for core MR1402-PC4 (red), which was correlated with the globally stacked LR04 $\delta^{18}O$ record (Lisiecki & Raymo, 2005) (gray). Red tick marks on the horizontal axis indicate tie points.

3. Methods

Magnetic susceptibility (*k*) was measured for all discrete samples by using a Kappabridge KLY-4S susceptometer. NRM was measured and subjected to a stepwise alternating-field (AF)

187 demagnetization at peak fields of 5, 10, 15, 20, 25, 30, 35, 40, 50, 60, and 80 mT. The
188 measurements were performed on alternate samples (290 in total) through core MR1402-PC4 by
189 using a pass-through cryogenic magnetometer (Model 760, 2-G Enterprises) at the Center for
190 Advanced Marine Core Research (CMCR), Kochi University, Japan. Principal component analysis
191 (PCA) (Kirschvink, 1980) was applied to the NRM demagnetization data to extract the
192 characteristic remanent magnetization component that reflects past geomagnetic field direction
193 (Figure 3). A range of 5 to 10 demagnetization steps was used for PCA, which was determined by
194 ensuring that the maximum angular deviation (MAD) (Kirschvink, 1980) was minimized. Fitting
195 was not anchored to the origin. Results for samples with MAD > 10° were discarded. After AF
196 demagnetization of the NRM, an ARM was imparted in a 0.1 mT direct current (DC) field with a
197 superimposed decaying AF with a peak field of 80 mT. The ARM was then subjected to stepwise
198 AF demagnetization at 10, 15, 20, 25, 30, 35, 40, 50, and 60 mT. Next, an IRM was imparted in a
199 2.5 T DC field with a pulse magnetizer (MMPM10, Magnetic Measurements) at CMCR, which is
200 treated here as SIRM. The SIRM was then demagnetized using the same stepwise peak AFs as the
201 NRM.

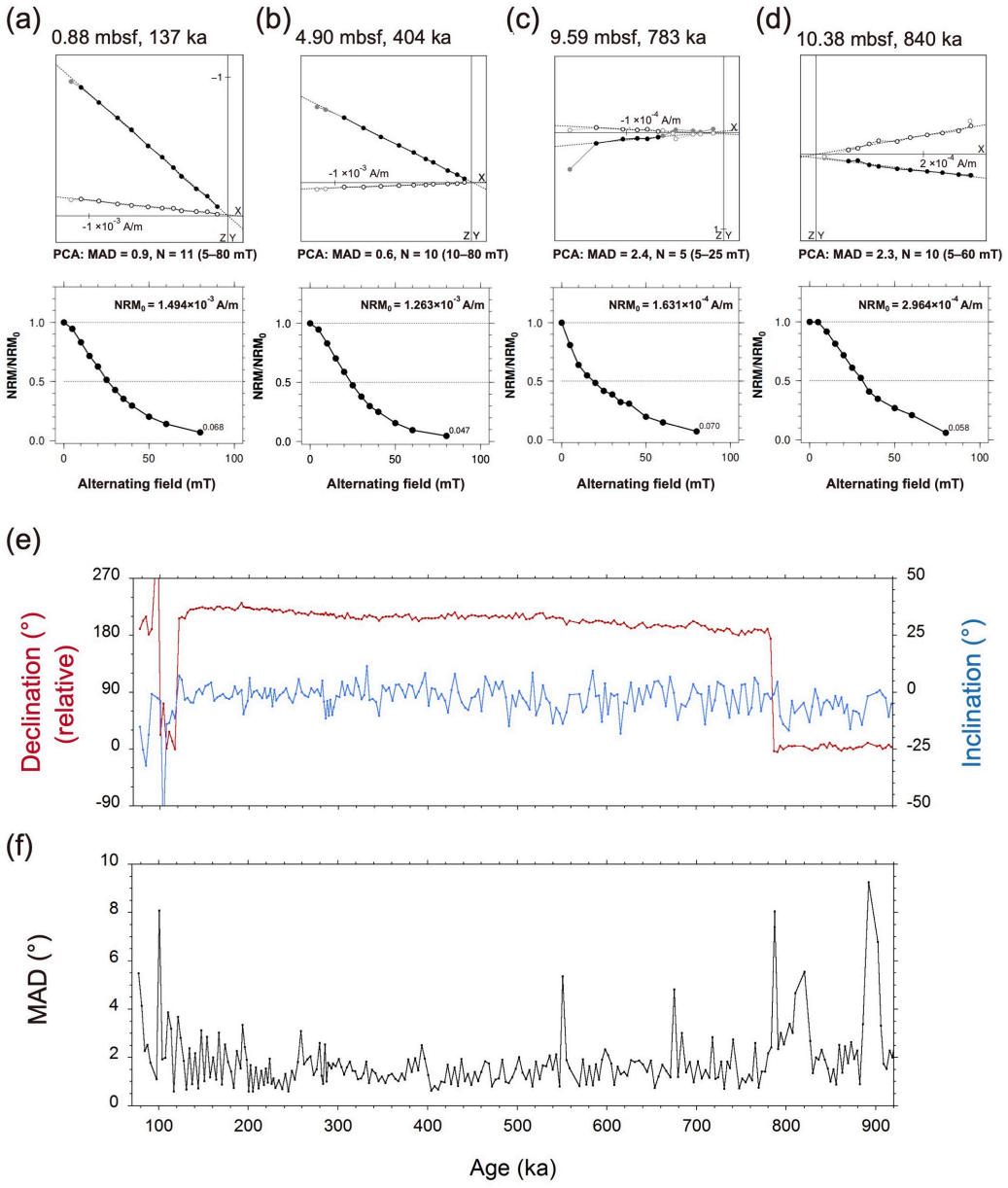

Figure 3. (a–d) Examples of stepwise AF demagnetization of NRM for (a, b) the Brunhes Chron, (c) just above the Matuyama–Brunhes polarity boundary, and (d) within the Matuyama Chron. Solid symbols are horizontal projections and open symbols are vertical projections of vector end points. N, number of demagnetization steps used for PCA; mbsf, meters below seafloor. (e)

Variations in relative declination (red) and inclination (blue) of NRM. (f) MAD values for PCA fits.

For RPI estimations, we tested both ARM and IRM as normalizers to compensate for variations in sediment magnetizability. First, for each sample, we constructed demagnetization diagrams between NRM–ARM pairs (Figure 4a–4c) and NRM–IRM pairs (Figure 4d–4f) at corresponding AF demagnetization steps. Then, we determined best-fit slopes to represent the RPI for each sample for each normalizer. The demagnetization interval of each best-fit slope was determined based on the conditions that three or more demagnetization steps must be used and that the highest correlation coefficient was chosen (Tauxe et al., 1995; Yamazaki & Yamamoto, 2018).

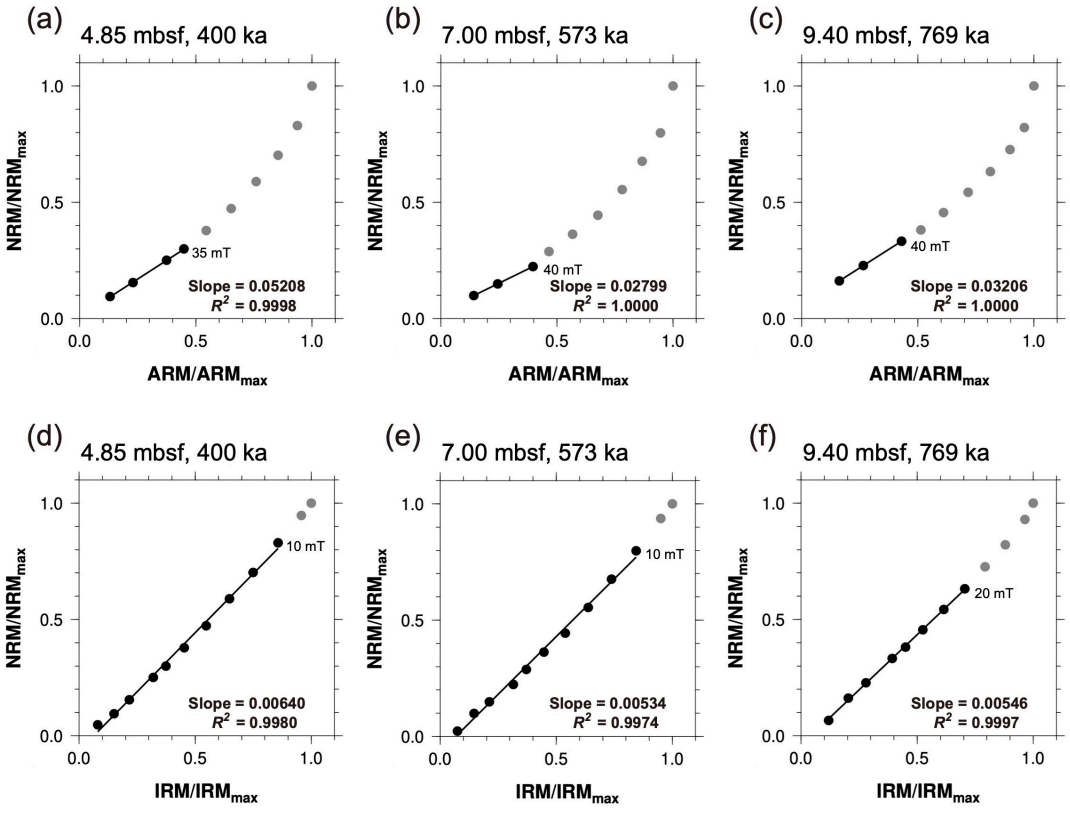

Figure 4. Examples of RPI estimations from best-fit slopes on (a–c) NRM–ARM demagnetization diagrams and (d–f) NRM–IRM demagnetization diagrams. AF demagnetization steps are indicated by solid circles. mbsf, meters below seafloor.

k_{ARM}/SIRM was calculated from the ARM and SIRM values obtained for RPI estimations; k_{ARM} was calculated by normalizing the ARM intensity with the strength of the applied DC field (0.1 mT). To determine the S-ratio, a 2.5 T IRM was first imparted using the impulse magnetizer.

Then, a backfield of 0.3 T was imparted in the direction opposite to the initial IRM. IRMs were measured using a spinner magnetometer (SMD88, Natsuhara-Giken) at CMCR. S-ratios were calculated according to the definition of Bloemendal et al. (1992):

$$S_{-0.3T} = \left(1 - \frac{IRM_{-0.3T}}{IRM_{2.5T}}\right)/2.$$

FORC measurements were made on five samples selected from core MR1402-PC4 at almost equal depth intervals. An alternating gradient magnetometer (AGM) (Flanders, 1988) (MicroMag 2900, Princeton Measurements Corporation) at the Atmosphere and Ocean Research Institute (AORI), The University of Tokyo, was used for these measurements. Samples were first dried overnight at room temperature. Then, samples of about 10 mg were attached to the AGM probe using silicon grease. Assuming that the magnetic minerals in our samples are dominated by SD magnetite, the coercivity (B_c) range was set to 0–100 mT. The range of the interaction field (B_u) was ±50 mT, which determines the upper and lower limits of the FORC diagrams. The saturating field was set to 1 T. The averaging time for each data point was 400 ms (800 ms for some weak samples) and the field increment was set to 2 mT. The number of FORCs was 111. FORC measurement data were analyzed using FORCinel software (Harrison & Feinberg, 2008) with VARIFORC smoothing protocol (Egli, 2013). The parameters used for smoothing were S_{c0} = 4, S_{b0} = 3, S_{c1} = S_{b1} = 7, and λ_c = λ_b = 0.1.

We obtained low-temperature magnetic measurements of two types on the same five samples that were used for the FORC measurements. For these measurements we used a low-temperature superconducting quantum interference device susceptometer (MPMS-XL5, Quantum Design) at CMCR. For the first measurement, an SIRM was imparted in a 3 T field at 300 K. Samples were then cooled to 10 K and then warmed back to 300 K in a nearly zero field. Magnetization changes were measured during the temperature cycling. For the second measurement, samples were cooled from 300 K to 10 K in a nearly zero field, then an SIRM was imparted by a 3 T field. Thermal demagnetization of the SIRM was measured during warming back to 300 K in a nearly zero field.

We obtained transmission electron microscope (TEM) observations to complement our rock-magnetic measurements. TEM observation can provide direct morphological and size information about magnetic-mineral assemblages in sediments. Although TEM observation

provides advantages compared to indirect rock-magnetic measurements, the results obtained from them remain semi-quantitative and may not faithfully reflect the overall morphology and size distribution of magnetic-mineral assemblages. Moreover, magnetic extraction is required before TEM observation, which can bias the information obtained. Nevertheless, TEM observations provide important information that supplements rock-magnetic measurements.

To extract magnetic minerals, the sediments were first dispersed in distilled water in an ultrasonic bath and circulated with a peristaltic tubing pump for about 24 h. Sodium hexametaphosphate was used as a deflocculant for the suspension. Magnetic minerals were extracted from the circulating suspension using a high magnetic field gradient produced by a strong magnet. The magnetic extracts were preserved in ethanol. Finally, a drop of the magnetic extracts–ethanol suspension was dried on a carbon-coated copper grid in preparation for TEM observation (Yamazaki & Yamamoto, 2018). A TEM (JEM-1400, JEOL) operated at 120 keV at AORI, was used for these observations.

To estimate the concentration of silicate-hosted magnetic-mineral inclusions in the studied sediments, and then to assess their contribution to paleomagnetic signal recording, quartz and feldspar were extracted from three selected samples using several geochemical procedures. Freeze-dried samples were weighed and treated with 1 N HCl to dissolve all carbonates and unprotected magnetic minerals, including magnetofossils. Sodium pyrosulfate ($Na_2S_2O_7$) fusion was then applied to separate quartz and feldspars from the samples (Blatt et al., 1982; Clayton et al., 1972; Stevens, 1991; Syers et al., 1968; Usui et al., 2018). Next, the samples were freeze-dried and heated gradually to 460 °C with $Na_2S_2O_7$ and then treated with 3 N HCl and washed with purified water. The residues were then heated to 50 °C in 0.5 M NaOH overnight and washed with purified water. Finally, the residues were freeze-dried and weighed again in preparation for further magnetic measurements. We assumed that any magnetic minerals that remained in the residues after these procedures were magnetic-mineral inclusions in quartz and feldspar. We estimated the contribution of silicate-hosted magnetic-mineral inclusions to paleomagnetic signal recording by comparing the SIRM magnitudes before and after extraction. SIRM was imparted using an impulse magnetizer (Model IM10-30, ASC Scientific) with a 2.7 T field and was measured using a spinner magnetometer (ASPIN, Natsuhara-Giken) at AORI. To estimate the coercivity distributions of the residues, FORC measurements were conducted using the aforementioned AGM at AORI. FORC measurement parameters were the same as those described above for the untreated samples.

4. Results and Interpretation

4.1. Paleomagnetic Directions

Stepwise AF demagnetization of the NRM generally reveals univectorial behavior, except for the first few demagnetization steps, which probably reflect a soft viscous remanent magnetization overprint that was removed at an AF of 10 mT for most samples (Figures 3a–3d). Paleomagnetic declinations and inclinations were determined by applying PCA (Kirschvink, 1980); MADs of less than 3° were obtained for most samples, except for those near a polarity transition (Figures 3e and 3f). Directional changes at around 100 ka are most likely caused by physical sediment disturbance during coring.

The Matuyama–Brunhes polarity transition appears as a ~180° relative declination flip (Figure 3e, red curve) at about 787 ka. There is a time lag of ~14 kyr relative to the recently proposed age of 773 ka for the Matuyama–Brunhes transition (Channell et al., 2020; Singer, 2014; Suganuma et al., 2018). This difference may be explained by delayed DRM lock-in. From the average sedimentation rate we estimated at the core location (~1.4 cm/kyr), we estimated the DRM depth-lag to be ~20 cm. We calculated the average inclination (excluding data at the polarity transition and the interval of physical disturbance) to be -0.54°, and obtained an inclination anomaly of -4.63° from the geocentric axial dipole field inclination (4.09°) at the site latitude. Our result is consistent with the known negative inclination anomaly of about -5° in the western equatorial Pacific (Johnson & Constable, 1997; Yamazaki et al., 2008). The observed high-quality paleomagnetic directional record of this core is a prerequisite for reliable RPI estimation.

4.2. Estimation of Relative Paleointensity

Before RPI estimation, it is preferable to check if the studied sediments satisfy empirical criteria for reliable RPI estimation, including relatively small variations in magnetic mineral concentrations and homogeneities of magnetic mineralogy and grain size (King et al., 1983; Tauxe, 1993). A gradual downcore magnetic mineral concentration decrease indicated by decreasing magnetic susceptibility (Figure 5a) reflects magnetic mineral dilution with increasing carbonate content. However, the magnetic concentration varies by less than an order of magnitude, which satisfies the empirical criteria (King et al., 1983; Tauxe, 1993). Variations of magnetic mineralogy and grain size can be estimated from bulk magnetic proxies, such as the S-ratio (mineralogy) and

312 k_{ARM}/SIRM (grain size). Sporadic drops of both of these proxies are evident in the studied
313 sediments (Figures 5b and 5c). Because high-coercivity magnetic minerals (e.g., hematite) are
314 more resistive to reductive diagenesis than low-coercivity minerals (e.g., magnetite) (Liu et al.,
315 2004; Yamazaki et al., 2003), the lower S-ratios we obtained (Figures 5b) may indicate reductive
316 dissolution of magnetite. Associated magnetic grain size increases indicated by k_{ARM}/SIRM drops
317 (Figures 5c) may also be attributed to the reductive dissolution of magnetite because fine grains
318 are expected to be dissolved earlier than coarse grains owing to their higher surface-to-volume
319 ratio (specific surface area). Therefore, in core MR1402-PC4, intervals in which magnetite
320 dissolution might have occurred (shaded in Figures 5a–5e) were excluded from RPI estimations
321 because they do not meet the empirical criteria of King et al. (1983) and Tauxe (1993).

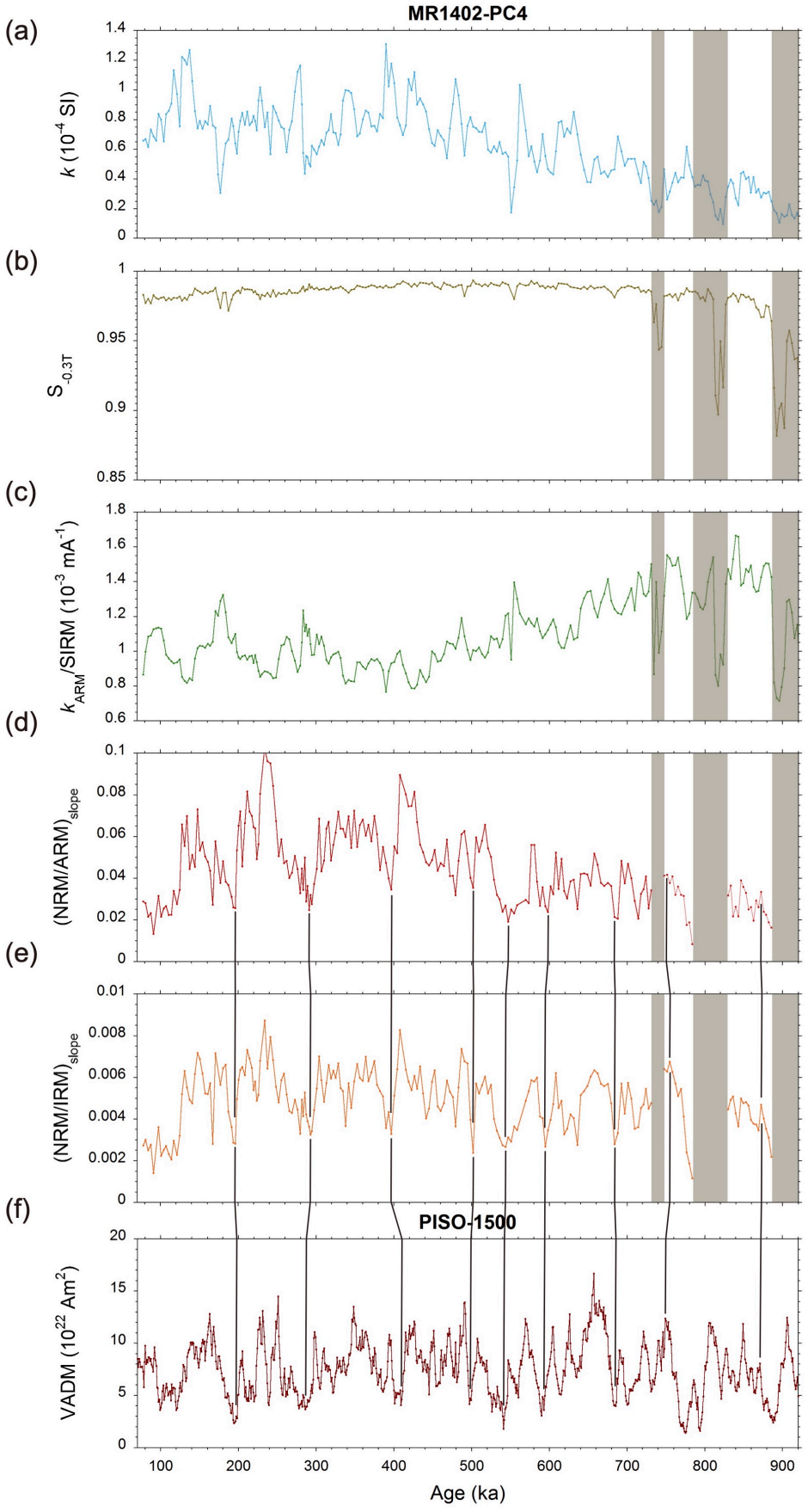
MR1402-PC4
(a)
k (10^{-4} SI)
(b)
$S_{-0.3T}$
(c)
k_{ARM}/SIRM (10^{-3} mA^{-1})
(d)
(NRM/ARM)$_{slope}$
(e)
(NRM/IRM)$_{slope}$
(f)
PISO-1500
VADM (10^{22} Am^2)
Age (ka)

322

Figure 5. Variations of (a) magnetic susceptibility (k), (b) S-ratio ($S_{-0.3T}$) and (c) ratio of k_{ARM} to SIRM in sediment core MR1402-PC4. Shaded intervals are likely affected by magnetite dissolution due to reductive diagenesis. RPI estimated from NRM intensity normalized by (d) ARM and (e) IRM. (f) The PISO-1500 paleointensity stack (Channell et al., 2009). VADM, virtual axial dipole moment. Correlations with the RPI records of core MR1402-PC4 are indicated by the tie lines in panels (d) to (f).

For RPI estimations, NRM intensities normalized by ARM and IRM (Figures 5d and 5e) were obtained from the best-fit slopes of NRM–ARM and NRM–IRM demagnetization diagrams (Figure 4). The PISO-1500 paleointensity stack (Channell et al., 2009; Figure 5f) was used as a template to assess the reliability of RPI estimations in this study. The overall patterns of the RPI records estimated from NRM intensity normalized by ARM (Figures 5d) and IRM (Figures 5e) agree reasonably well with the PISO-1500 paleointensity stack of Channell et al. (2009; Figures 5f). However, RPI normalized by ARM (NRM/ARM) (Figure 5d) has a conspicuous artificial downcore decrease, especially in the lower part of the core, whereas RPI normalized by IRM (NRM/IRM) (Figure 5e) does not. Intriguingly, k_{ARM}/SIRM has an approximate inverse correlation with the RPI normalized by ARM (compare Figures 5c and 5d), indicated by correlation coefficient $\rho = -0.55$ and statistical significance $P < 0.01$. This approximate inverse correlation is also evident in a biplot of k_{ARM}/SIRM and NRM–ARM slope (Figure S1), where the amplitude of NRM–ARM slope is subdued with increasing k_{ARM}/SIRM. This approximate inverse correlation suggests that the relative proportion of biogenic to terrigenous magnetic components in the sediments increases with depth and that ARM fails to compensate for compositional changes. Comparison of the downcore variations of ARM and SIRM (Figure S2) support this interpretation. SIRM decreases consistently with magnetic susceptibility (Figure 5a), reflecting magnetic concentration changes, whereas ARM exhibits a gentler downcore decrease. These observations indicate that changes in ARM acquisition efficiency are responsible for the approximate inverse correlation between the ARM-normalized RPI and the k_{ARM}/SIRM. Therefore, we consider IRM to be a more appropriate normalizer than ARM for the studied sediments. Inverse correlations between RPI and k_{ARM}/SIRM has been reported for sediments from various regions (Hofmann & Fabian, 2009; Sakuramoto et al., 2017; Yamazaki et al., 2013; Yamazaki & Yamamoto, 2018). This could be attributed to differences in remanence acquisition efficiency between biogenic and terrigenous components (Yamazaki et al., 2013).

We obtained curved slopes in NRM–ARM demagnetization diagrams (Figures 4a–4c). When all NRM-ARM pairs are plotted on a single demagnetization diagram (Figure 6a), a similar curved trend is evident; in contrast, NRM–IRM demagnetization diagrams show an approximately linear relationship (Figure 6b). The curvatures suggest that NRM and ARM have different coercivity distributions. ARM acquisition is more efficient for SD biogenic magnetite, whereas terrigenous magnetic minerals are likely to include vortex and/or MD grains. Consequently, biogenic and terrigenous components will have different acquisition efficiencies for NRM and ARM. Therefore, the curvature in NRM–ARM demagnetization diagrams can be attributed to mixtures of biogenic and terrigenous magnetic mineral components.

To attempt to separate the different contributions of biogenic and terrigenous components to RPI signals, we re-calculated best-fit slopes on NRM–ARM demagnetization diagrams for two AF demagnetization intervals: a low-coercivity window of 10–25 mT and a high-coercivity window of 35–60 mT (Figure 7a–7c), following the methods of Ouyang et al. (2014) and Chen et al. (2017). These coercivity intervals were selected to separate and optimize the fit of curves in the NRM–ARM demagnetization diagrams (average R^2 = 0.99 for the low-coercivity window with standard deviation < 0.02 and average R^2 = 0.96 for the high-coercivity window with standard deviation < 0.1).

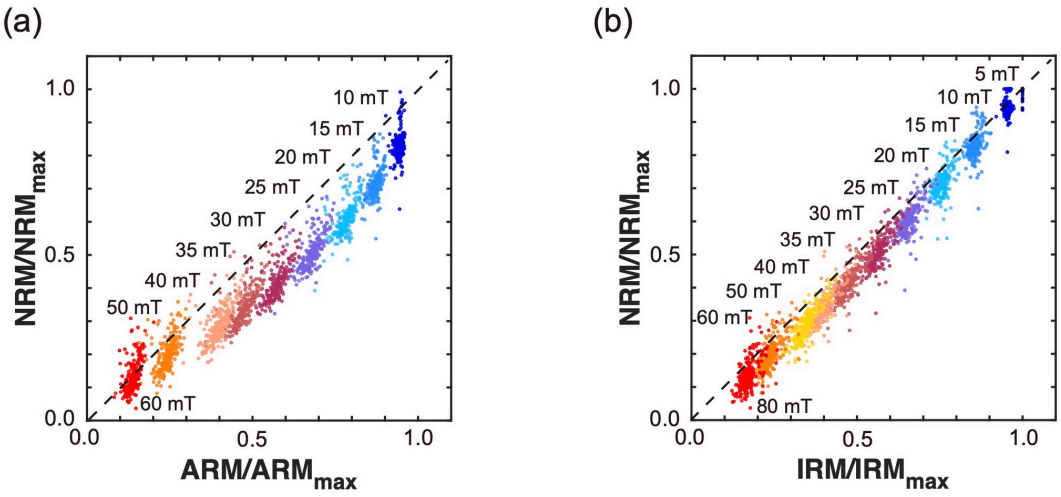

Figure 6. Demagnetization data for (a) NRM–ARM and (b) NRM–IRM pairs at various (color-coded) AF demagnetization steps (mT). Dashed lines indicate 1:1 relationships.

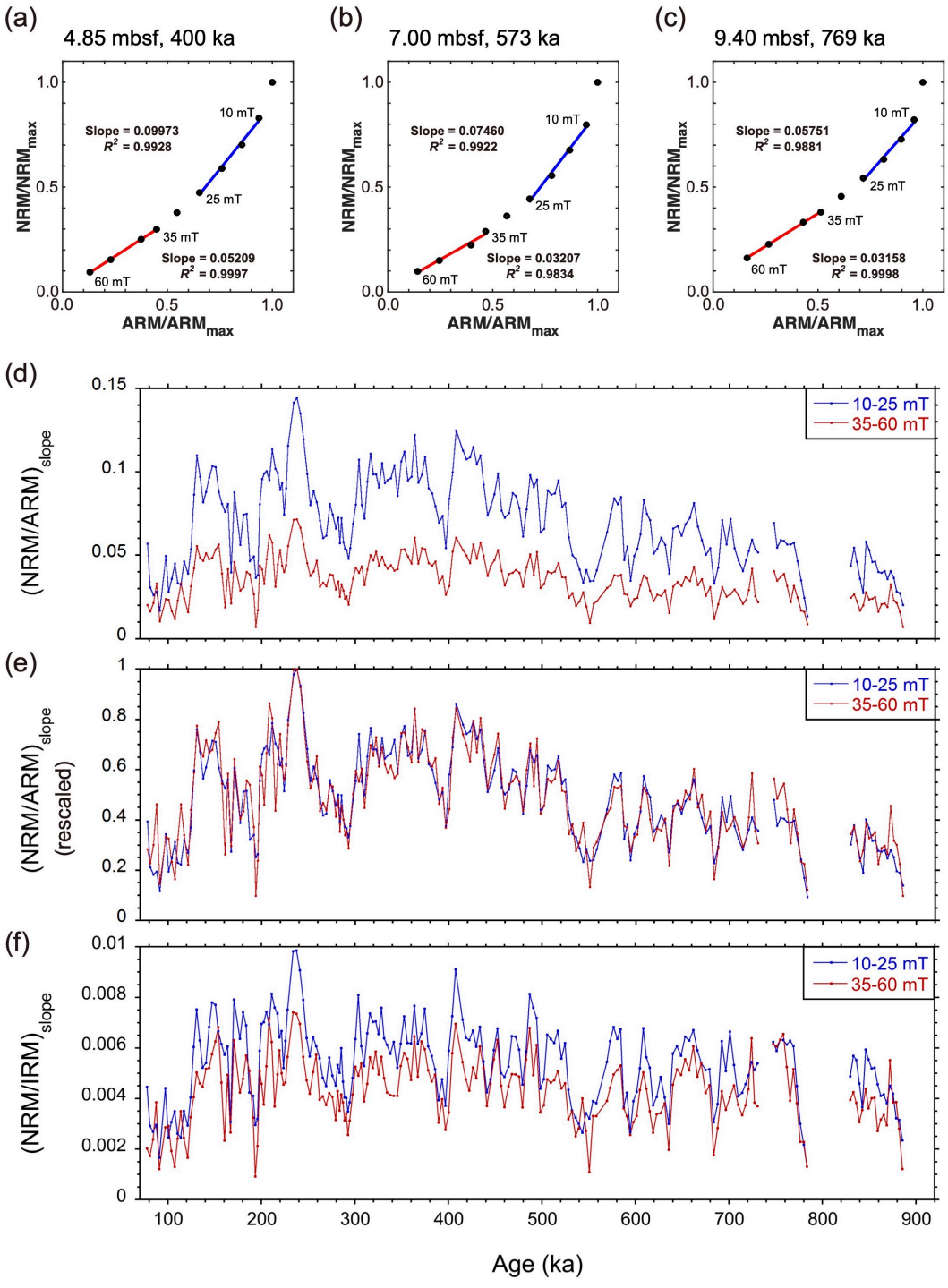

Figure 7. Examples of best-fit slopes for (a–c) NRM–ARM demagnetization diagrams calculated for AF demagnetization intervals of 10–25 mT (red lines) and 35–60 mT (blue lines).

RPI signals calculated for the same coercivity windows for (d, e) NRM–ARM slope and (f) NRM–IRM slope. In panel (e) both RPI curves were rescaled by their maximum values.

ARM-normalized RPIs within the high-coercivity window are smaller than those in the low-coercivity window (Figure 7d); however, paleointensity variations for the two windows are concordant after rescaling (Figure 7e). The downcore artificial decreases for the two coercivity windows are also identical. For NRM normalized by IRM (Figure 7f), differences in RPI estimated from the two coercivity windows are smaller than for the ARM normalization, but normalized intensities for the low-coercivity window are still marginally higher than those for the high-coercivity window. These differences are also evident in Figure 6b, where the low-coercivity data clusters are closer to the 1:1 line, but the high-coercivity data clusters plot below it.

4.3. FORC Diagrams

Previous research demonstrated that intact magnetosome chains produced by MTB can have similar magnetic properties to those of uniaxial non-interacting SD particles. The latter produces a distinct ridge-like FORC distribution along the B_c axis with almost no vertical spread (known as the central ridge) and a subsidiary negative peak along the negative B_u axis near $B_c = 0$. Hence, its contribution can be isolated easily from magnetic-mineral assemblages using FORC diagrams (Egli, 2021; Egli et al., 2010; Pike et al., 1999; Roberts et al., 2000, 2012, 2014; Yamazaki, 2008, 2009; Yamazaki & Ikehara, 2012). The spread of the central ridge along the B_c axis represents the coercivity distribution of the magnetic particles and is clearly identifiable even in complex mixtures with other magnetic components. Central ridges are clearly evident in FORC diagrams for the measured samples (Figure 8a). The coercivity distributions of all samples extend to about 60 mT or higher, which corresponds to the high-coercivity component of NRM–ARM slopes. The FORC distributions also have a component with a significant vertical spread, with outer contours that diverge toward the B_u axis. This component can be attributed to interacting SD, vortex and/or MD particles, which are likely carried by the terrigenous magnetic-mineral component. The central-ridge FORC distributions of biogenic magnetite origin were extracted from the total FORC distributions (Figure 8b) by using the FORCinextras function in the FORCinel software (Harrison & Feinberg, 2008), in which the central ridge signal can be calculated by subtracting a smoothed and extrapolated "ridge-free" background FORC distribution from an original FORC distribution. The detailed mathematical foundation of this approach was

explained by Egli et al. (2010). The integrals of these identifiable FORC distributions over specified FORC regions are defined as FORC magnetizations of corresponding magnetic components (Egli et al., 2010). Because the integral of the total FORC distribution over the memory region coincides with the integral of the DC demagnetization curve (f_{dcd}), which is alternatively equivalent to the saturation remanent magnetization (M_{rs}) (Egli, 2021; Pike, 2003), the ratio between the integral of the extracted central-ridge FORC distribution (M_{cr}) and the calculated M_{rs} can be used to roughly estimate the relative contribution of the biogenic magnetite to the remanent magnetization of the sediments.

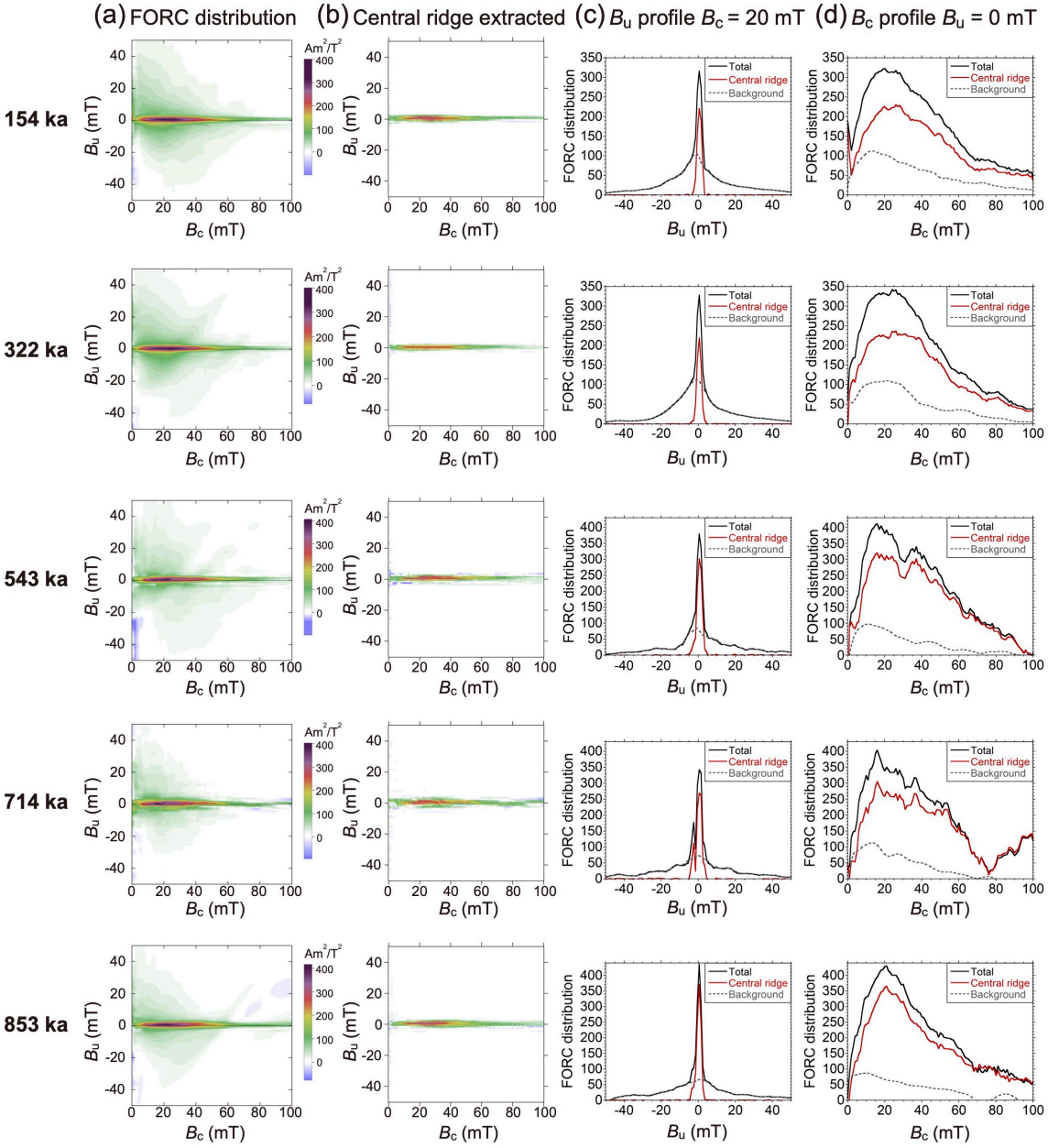

Figure 8. (a) FORC diagrams for five samples from core MR1402-PC4, (b) the central ridge component extracted from each FORC diagram, (c) profiles of interaction field (B_u) distributions at coercivity (B_c) of 20 mT, and (d) profiles of coercivity distributions at $B_u = 0$. In panels (c) and (d), profiles of the central-ridge component (red), the background component (gray), and the total (black) are shown.

We estimated the relative contribution of biogenic magnetite for the low- (10–25 mT) and high- (35–60 mT) coercivity windows separately from the FORC magnetizations of the corresponding B_c windows (Figure 9a). Biogenic magnetite contribute more to the remanent magnetization in the high-coercivity window than that in the low-coercivity window (Figure 9b). The difference in these contributions is greater in the deeper part of the core, where biogenic magnetite in the high-coercivity window contributes up to 40% of the total remanent magnetization. The relative proportion of biogenic magnetite that we calculated should be considered as a minimum estimate, because magnetosomes in multi-stranded configurations and in bent or fold-collapsed chains can yield vertical spreads that are nearly symmetrical around the central ridge in FORC diagrams (Amor et al., 2022; Berndt et al., 2020; Chang et al., 2019; Inoue et al., 2021; Li et al., 2012; Usui & Yamazaki, 2021), which is counted as the terrigenous component in our calculation. The relative contributions of biogenic magnetite to the remanent magnetization in both coercivity windows increase with depth, which is consistent with the downcore k_{ARM}/SIRM increase, and indicates an increasing relative abundance of biogenic magnetite. These results suggest that the remanent magnetization in the high-coercivity window is carried more by biogenic magnetite. Therefore, the high-coercivity component in RPI estimations corresponds mainly to biogenic magnetite, whereas terrigenous magnetic minerals dominate the low-coercivity component.

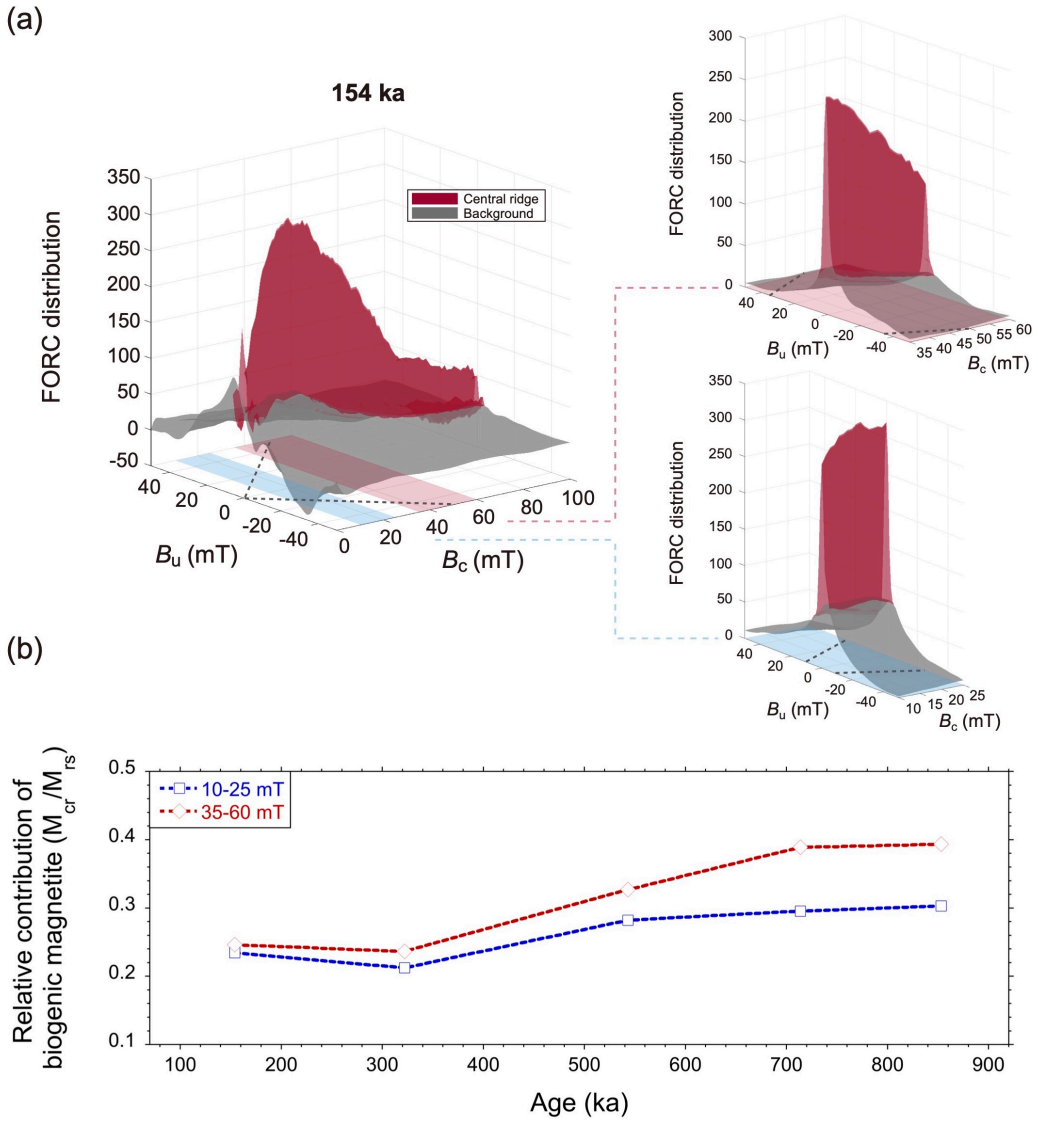

Figure 9. Relative contribution of biogenic magnetite to the remanent magnetization of the sediments. (a) Schematic illustration of the estimation process, which is based on the ratio of the integral of the extracted central-ridge FORC distributions (M_{cr}) to the integral of the total FORC distributions over the memory region (M_{rs}). Areas within dashed lines define the memory region. (b) Results for five samples from core MR1402-PC4, estimated from the high-coercivity window in red (35–60 mT) and from the low-coercivity window in blue (10–25 mT).

4.4. Low-temperature magnetic measurements

The Verwey transition (Verwey, 1939) temperature (T_v) at around 100 K was observed in zero-field SIRM warming curves (red curves in Figure 10b) for all five analyzed samples. This is

449 easier to recognize in derivative curves (orange curves in Figure 10b). Two distinct peaks at ~95
450 K and ~115 K (or broad bell-shaped peaks) are observed in the derivative curves. The lower T_v is
451 reported to be an intrinsic property of biogenic magnetite (Chang, Heslop, et al., 2016; Li et al.,
452 2009; Pan et al., 2005); therefore, the presence of two T_v peaks suggests that the studied sediments
453 are a mixture of biogenic and terrigenous inorganic magnetites.

454 The degree of maghemitization can be estimated from the low-temperature cycling curves
455 of SIRM at 300 K (Figure 10a). When temperature decreases from 300 K to T_v, the SIRM of
456 magnetite acquired at 300 K decreases, whereas that of maghemite increases monotonically. Thus,
457 low-temperature cycling curves for magnetite with oxidized maghemite surfaces can be considered
458 to be a superposition of the two curves (Özdemir & Dunlop, 2010) and maghemitization can be
459 assessed by comparing the magnetization at 300 K with that below T_v at, for example, 50 K (Chang
460 et al., 2013; Yamazaki & Solheid, 2011). The magnetization at 300 K is greater than that at 50 K
461 in most samples (Figure 10a), indicating a relatively low degree of maghemitization (Chang et al.,
462 2013; Özdemir & Dunlop, 2010), which is consistent with the Fe-redox boundary recognized at
463 ~20 cm depth in the core. For the deepest sample (at 853 ka), the magnetization at 50 K is slightly
464 larger than that at 300 K. Considering the low magnetite concentration at that depth, as indicated
465 by the low magnetic susceptibility (Figure 5a), this result might be due to the influence of
466 paramagnetic minerals and the presence of a small residual field in the MPMS during measurement.

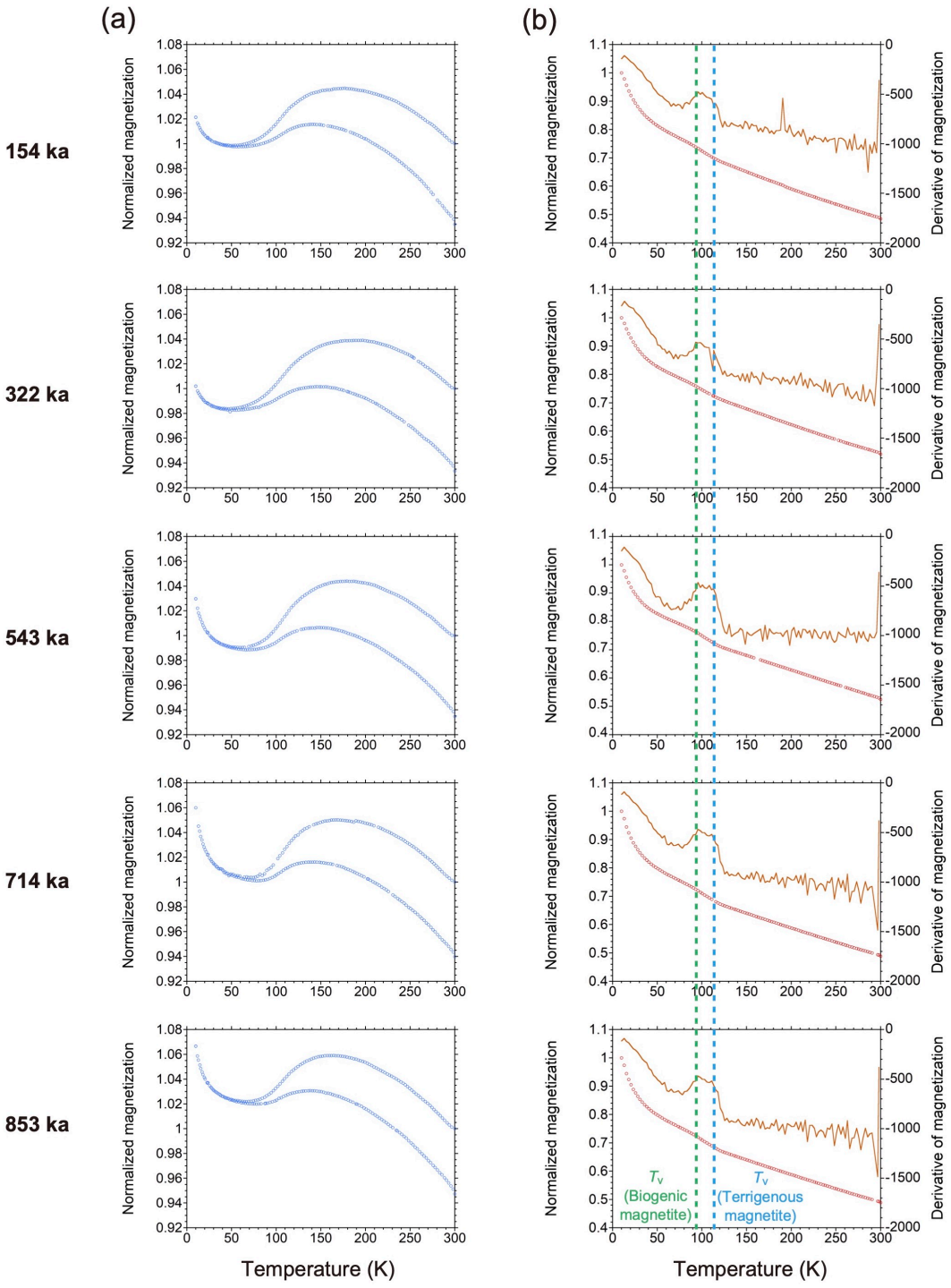

Figure 10. Results of low-temperature magnetic measurements for five samples from core MR1402-PC4. Low-temperature cycling curves (a) normalized by SIRM at 300 K (blue); (b)

zero-field warming curves normalized by SIRM at 10 K (red), with derivative of the curves in orange. Verwey transition temperature peaks (T_v) are also shown in panel (b).

4.5. TEM Observations

TEM observations were conducted on magnetic-mineral extracts from two samples (at 322 and 853 ka). In total, more than 2380 magnetofossils were identified in hundreds of TEM images. We recognized magnetofossils of three distinct morphologies: equant (cubo-octahedra and hexagonal prisms where length-to-width ratios are close to one); elongated (hexagonal prisms and elongated octahedra); and bullet-shaped magnetofossils (Akai et al., 1991; Bazylinski et al., 1994; Li et al., 2020; Yamazaki, 2020) (Figure 11). The bullet-shaped morphology is prismatic with one end tapered and curved sides and is easily distinguished from the other magnetofossil types. The elongated type occurs commonly as a hexagonal prism or elongated octahedron. We considered some of the hexagonal prisms (those with length-to-width ratios close to one) to have magnetic properties similar to those of the cubo-octahedra, owing to their small shape anisotropy. However, there are inherent ambiguities in the classification of the three-dimensional morphologies of magnetofossils from projected two-dimensional TEM images (e.g., the axial ratios of magnetofossils vary continuously and at certain angles an elongated octahedron can have a similar two-dimensional projection to that of an equant octahedron); thus, this type of characterization is semi-quantitative.

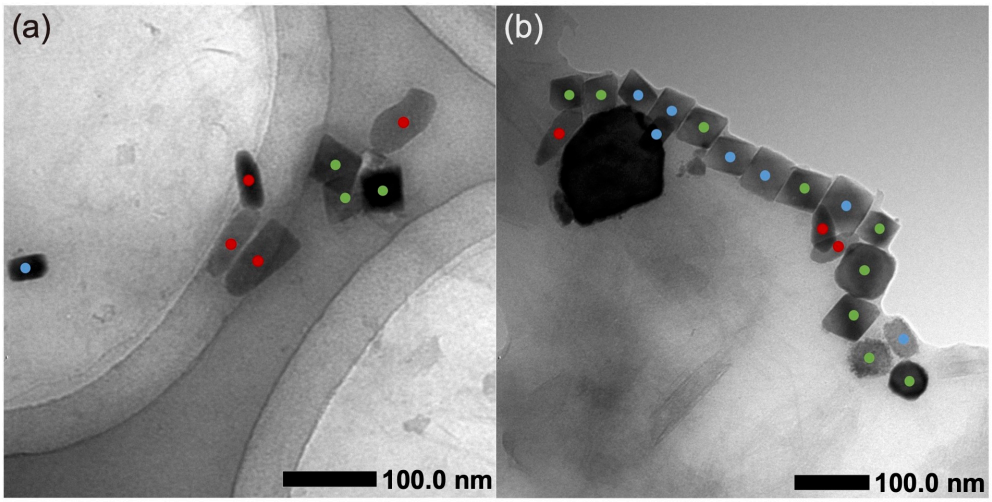

Figure 11. TEM images of magnetic extracts from core MR1402-PC4 (a) at 3.82 m (322 ka) and (b) at 10.57 m (853 ka). Red, blue, and green dots identify bullet-shaped, elongated, and equant magnetofossils, respectively.

The coercivity of intact biogenic magnetite chains is controlled by the shape anisotropy of the magnetite particles as well as by the chain configuration, such as the number of magnetite particles and by the bending angle in a chain structure (Berndt et al., 2020; Chang et al., 2019; Li et al., 2013; Paterson et al., 2013). Nevertheless, the abundance of anisotropic biogenic magnetite shapes in sediments tends to correlate with relatively high coercivities (Lascu & Plank, 2013; Usui et al., 2017; Yamazaki, 2012; Yamazaki et al., 2020; Yamazaki & Ikehara, 2012). Our magnetofossil count results for the three morphologies (Table 1) indicate that the anisotropic morphology groups (elongated and bullet-shaped magnetofossils) consist of more than 50% of the magnetofossils in our two samples, which supports the observation from FORC diagrams that the central ridge due to biogenic magnetite extends to higher coercivities.

Table 1. Counts of magnetofossil morphologies from TEM observations.

Age of samples (ka)	Bullet-shaped	Elongated	Equant	Total
322	378 *(24%)*	463 *(29%)*	734 *(47%)*	1575 *(100%)*
853	156 *(19%)*	291 *(36 %)*	358 *(45%)*	805 *(100%)*

4.6. Silicate-Hosted Magnetic-Mineral Inclusions

The contribution of silicate-hosted magnetic-mineral inclusions to RPI signals was assessed by comparison of the SIRM values of the untreated samples with those of the residues of chemical extraction procedures (Table 2). The mass fractions of the residues are less than 2% of the untreated sediment samples, and account for less than 7% of SIRM. These results indicate that the contribution of the silicate-hosted magnetic-mineral inclusions to the RPI signal recording is smaller than that of biogenic magnetite and unprotected terrigenous magnetic minerals. The magnetite particle concentration within the host silicate minerals can be roughly estimated as follows. Considering that the saturation magnetization of magnetite is 92 Am^2/kg (O'Reilly, 1984), and if it is assumed that the magnetite particles are all uniaxial SD particles randomly oriented in the host silicate minerals, then, based on Stoner & Wohlfarth (1948) theory, the SIRM of the

514 magnetite particles in the silicates should be 46 Am^2/kg. Compared to the mass-normalized SIRM
515 of the residues in Table 2, the magnetic particle concentration is of the order of 0.01%. Preferred
516 crystallographic orientations are common in exsolved inclusions and can cause variations of
517 remanent magnetization from 25% to 100% as a function of applied field orientation (Feinberg et
518 al., 2006). Therefore, the actual contribution of the inclusions to the RPI signals would be smaller,
519 and the magnetite particle concentration would be in the range 0.001%–0.01%.

520 **Table 2.** Comparison between properties of samples before and after the chemical extraction of
521 quartz and feldspar.

Depth (m)	Age (ka)	Bulk SIRM of untreated samples (10^{-6} Am^2)	Bulk SIRM of residues (10^{-6} Am^2)	Magnetization fraction of residues (%)	Mass fraction of residues (%)	Mass-normalized SIRM of untreated samples (10^{-3} Am^2/kg)	Mass-normalized SIRM of residues (10^{-3} Am^2/kg)
4.57	378	9.62	0.51	5.25	1.75	1.77	5.32
7.95	649	4.84	0.15	3.03	1.44	0.92	1.94
10.43	843	2.89	0.20	6.78	1.30	0.50	2.61

522 FORC diagrams for the residues after chemical extraction of quartz and feldspar have a
523 peak near the origin (i.e., $B_u = 0$, $B_c = 0$) (Figure 12a), which indicates that a large amount of the
524 magnetic inclusions have sizes near the SP/SD boundary (Pike et al., 2001) as well as of SD and
525 vortex state particles. In addition, high-coercivity FORC signals in the residues are smaller than
526 those of the original samples (Figure 8a).

527 TEM observation was conducted on the residues at 378 ka as a complement to FORC
528 analyses (Figures 12b and 12c). The TEM used here does not have an energy-dispersive
529 spectrometer, so we could not identify the mineralogy of the inclusions. However, magnetic
530 inclusions commonly appear as dark particles in TEM images. The dark particles included in the
531 transparent minerals in Figure 12, which are likely magnetite within silicates, range in size from a
532 few nanometers to tens of nanometers, which is consistent with the SP/SD as well as SD and vortex
533 state FORC signatures (Figure 12a). SP particles do not contribute to SIRM in our calculation of
534 the magnetite particle concentration within the host silicate minerals, so the actual magnetite
535 particle concentration would be larger.

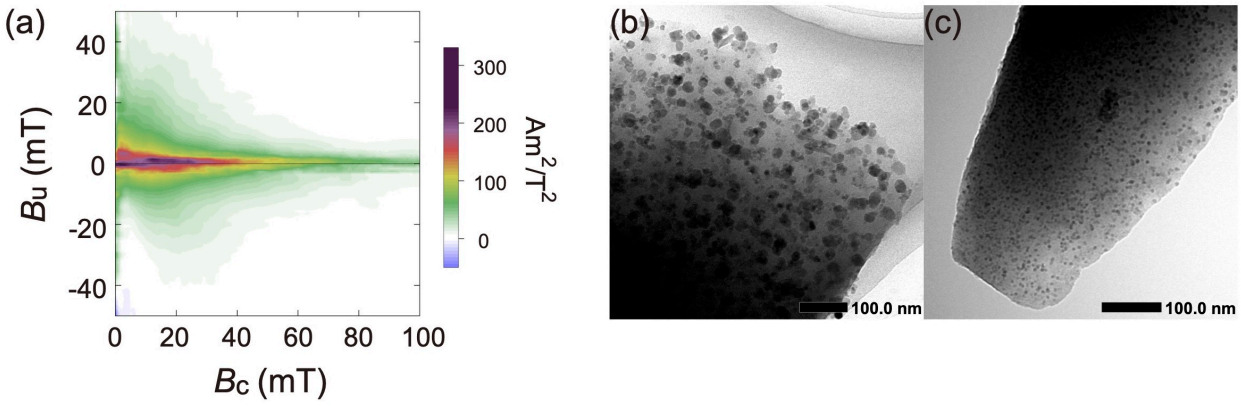

536

537 **Figure 12**. (a) FORC diagram and (b, c) TEM images of silicate-hosted magnetic-mineral
538 inclusions extracted from core MR1402-PC4 at 4.57 m (378 ka).

539 **5. Discussion**

540 Results from FORC measurements indicate that the RPI records of the studied sediments
541 in the high-coercivity window has a larger contribution from biogenic magnetite than those in the
542 low-coercivity window. TEM observations on magnetofossils suggest that elongated
543 magnetofossils could have higher coercivities. Maghemitization processes might contribute to the
544 high-coercivity component. Low-temperature oxidation proceeds inward from the surface of a
545 magnetite grain to produce a fully oxidized maghemite shell that grades gradually into a largely
546 unoxidized magnetite core. This gradient of oxidation degree can induce stresses, and hence the
547 coercivity of a magnetite grain should increase with increasing maghemitization (Cui et al., 1994;
548 van Velzen & Zijderveld, 1995). However, our observarions on low-temperature magnetic
549 measurements indicate that the degree of maghemitization is relatively low in the studied
550 sediments. Maghemitization, therefore, is not the likely source of the high-coercivity component.
551 Silicate-hosted magnetic inclusions could be considered a candidate carrier of the high-coercivity
552 component. However, FORC diagrams of the residues after chemical extraction procedures
553 (Figure 12a) show smaller high-coercivity FORC signals than those of the untreated samples
554 (Figure 8a), so the silicate-hosted magnetic inclusions are also unlikely to be the carrier of the
555 high-coercivity signal. We therefore consider biogenic magnetite to be the dominant high-
556 coercivity signal carrier with additional unprotected terrigenous magnetic minerals in the studied
557 sediments.

The ARM-normalized RPI records estimated from the high- and low-coercivity windows indicate that biogenic magnetite has a lower RPI compared to the terrigenous component (Figure 7d). This difference is also evident when RPIs from the high-coercivity window are plotted against those from the low-coercivity window (Figure S3a), where most of the NRM/ARM data fall below the 1:1 line, indicating the higher RPI recording efficiency of the terrigenous component. The NRM intensity normalized by ARM of the terrigenous component is at least 1.5–2.5 times higher than that of the biogenic component. This difference can be explained by RPI underestimations owing to increasing ARM acquisition efficiency with increasing biogenic magnetite proportion. Note that RPI signals from both the high- and low-coercivity windows have identical artificial downcore decreases that correlate with a downcore k_{ARM}/SIRM increase (Figures 5c and 7e). These correlations indicate that the RPI signals of the low-coercivity window are also influenced by increasing biogenic magnetite proportion in the sediments.

Concave-down curvatures in NRM–ARM demagnetization diagrams and distorted RPI variations that correlate with k_{ARM}/SIRM indicate that ARM normalization is not appropriate for RPI estimation in these sediments, even for the low-coercivity window. However, for NRM normalized by IRM, the difference of the RPI recording efficiencies for biogenic and terrigenous components is lower than that for ARM normalization (Figure S3b), but the low-coercivity terrigenous component still has higher RPI recording efficiency than the biogenic component. The terrigenous component is at least 1–1.5 times more efficient than the biogenic component in RPI recording. These observations emphasize that accurate RPI estimations require magnetically homogeneous sediments.

Chen et al. (2017) used methods similar to ours to investigate the RPI recording efficiency of various magnetic components in sediment cores from the eastern equatorial Pacific Ocean. They used several analyses (including FORC diagrams, IRM unmixing, and TEM observations) to identify two types of dominant stable SD components that correspond to biogenic magnetite in high-coercivity distribution and terrigenous magnetic particles in low-coercivity distribution. They argued that the silicate-hosted magnetic inclusions that dominate the low-coercivity terrigenous component are mainly of SD size and are present at concentrations sufficiently high to be detectable in magnetic measurements. They then compared the ARM-normalized RPIs of the high- and low-coercivity windows while assuming that biogenic magnetite corresponds to the higher coercivity component and silicate-hosted magnetic inclusions correspond to the lower coercivity

component. Their result is contrary to our findings (Chen et al., 2017, their Figure 8): their NRM–ARM demagnetization diagrams have convex curvatures, and the biogenic component carries a stronger RPI signal.

Possible reason for the contradiction with the study of Chen et al. (2017) might be different concentrations of silicate-hosted magnetic inclusions in sediments from different environments. The contribution of eolian dust to sediments in the western equatorial Pacific Ocean site of core MR1402-PC4 is small (Rea, 1994; Winckler et al., 2016; Wu et al., 2013). Terrigenous particles in this region are considered to be mainly of fluvial origin from New Guinea (Dang et al., 2020; Wu et al., 2013). The silicate-hosted magnetic inclusion mass-fraction concentration in core MR1402-PC4 is less than 2%, and carries less than 7% of SIRM (Table 2). Therefore, terrigenous magnetic minerals in our study would be mainly unprotected magnetic particles in the interacting SD, vortex, and/or MD states. The core site of Chen et al. (2017) is from a different oceanographic regime, and can receive eolian dust from the Americas (Rea, 1994) or from Asia, depending on the position of the intertropical convergence zone (Yamazaki, 2012). If such dust contains more silicate-hosted magnetic inclusions and/or less unprotected magnetite per unit volume than the fluvival particles from New Guinea, then silicate-hosted magnetic inclusions might dominate the terrigenous magnetic minerals. In this case, the contradiction can be explained by assuming that the RPI recording efficiency of terrigenous magnetic minerals other than silicate-hosted magnetic inclusions is higher than that of biogenic magnetite, whereas the RPI recording efficiency of silicate-hosted magnetic inclusions is lower than that of biogenic magnetites. Some studies have suggested that silicate-hosted magnetic inclusions possess low RPI recording efficiency or even cannot preserve reliable RPI signals (Chang et al., 2021; Chang, Roberts, et al., 2016; Hong et al., 2019). Regardless, the apparent contradiction implies that compositional differences in sediments from different geological environments can influence remanent magnetization acquisition efficiency. More research is needed to further investigate this issue.

6. Conclusions

Our paleo- and rock-magnetic study of core MR1402-PC4 sediments from the Ontong Java Plateau in the western equatorial Pacific led us to the following conclusions.

1. A downcore increase of the ratio of biogenic to terrigenous magnetic minerals was estimated using k_{ARM}/SIRM. The ratio correlates negatively with RPI normalized by ARM, which

suggests that ARM normalization failed to compensate for compositional changes in the sediments.

2. RPIs calculated in high- and low-coercivity windows of NRM–ARM and NRM–IRM demagnetization diagrams indicated that the high-coercivity portion has smaller RPI than the low-coercivity portion. From FORC diagrams, TEM observations, low-temperature measurements, and the extraction of silicate-hosted magnetic inclusions, we showed that NRM in the high-coercivity window is carried more by biogenic magnetite, whereas NRM in the low-coercivity window is carried more by terrigenous magnetic minerals. Thus, the RPI recording efficiency of biogenic magnetite is lower than that of the terrigenous component.
3. Previous studies have used similar methods to indicate higher RPI recording efficiency for biogenic magnetite, which is contrary to our conclusion. Different magnetic mineral components have different RPI recording efficiencies, so different silicate-hosted magnetic inclusion concentrations in different sedimentary environments are likely to be responsible for the observed differences among these studies.

Data Availability Statement

All data produced in this study are available from the Zenodo repository (https://doi.org/10.5281/zenodo.6351605).

Acknowledgments, Samples, and Data

The core used in this study was obtained with the cooperation of all onboard scientists, officers, and crew of R/V *Mirai* MR14-02 cruise and on-shore personnel related to the cruise. We thank Toshihiro Yoshimura and Haruka Takagi for their help with onboard sampling. We also thank Yuhji Yamamoto for support with the paleo- and rock-magnetic measurements and for providing the software used to process demagnetization data, Yosuke Miyairi for help with geochemical extraction of silicate-hosted magnetic inclusions, and Nobuhiro Ogawa for technical assistance with TEM observations. We thank Andrew P. Roberts, an anonymous reviewer, the Editor Mark Dekkers and an Associate Editor for their thoughtful and constructive comments that greatly improved this paper. This study was partly conducted under the cooperative research program of the Center for Advanced Marine Core Research, Kochi University (19A024 and 19B022) and was partly supported by the Japan Society for the Promotion of Science (JSPS) KAKENHI Grant

numbers 15K21221, 18H01279, and 19H01997; the Japan−Germany Research Cooperative Program between JSPS and the Deutscher Akademischer Austauschdienst, Grant number JSPSBP1 20203510; and Kanazawa University SAKIGAKE Project 2020. The work of Jiaxi Li was supported by the China Scholarship Council, Grant number 202108050144.

References

Akai, J., Sato, T., & Okusa, S. (1991). TEM Study on Biogenic Magnetite in Deep-sea Sediments from the Japan Sea and the Western Pacific Ocean. In *Electron Microsc* (Vol. 40).

Amor, M., Wan, J., Egli, R., Carlut, J., Gatel, C., Andersen, I. M., Snoeck, E., & Komeili, A. (2022). Key Signatures of Magnetofossils Elucidated by Mutant Magnetotactic Bacteria and Micromagnetic Calculations. *Journal of Geophysical Research: Solid Earth*, *127*(1), e2021JB023239. https://doi.org/https://doi.org/10.1029/2021JB023239

Banerjee, S. K., King, J., & Marvin, J. (1981). Environmental Studies*. In *Geophysical Research Letters* (Vol. 8, Issue 4).

Bazylinski, D. A., Garratt-Reed, A. J., & Frankel, R. B. (1994). Electron microscopic studies of magnetosomes in magnetotactic bacteria. *Microscopy Research and Technique*, *27*(5), 389–401. https://doi.org/10.1002/jemt.1070270505

Berndt, T. A., Chang, L., & Pei, Z. (2020). Mind the gap: Towards a biogenic magnetite palaeoenvironmental proxy through an extensive finite-element micromagnetic simulation. *Earth and Planetary Science Letters*, *532*. https://doi.org/10.1016/j.epsl.2019.116010

Blatt, H., Jones, R. L., & Charles, R. G. (1982). Separation of quartz and feldspars from mudrocks. *Journal of Sedimentary Research*, *52*(2), 660–661. https://doi.org/10.2110/jsr.52.660

Bloemendal, J., King, J. W., Hall, F. R., & Doh, S. J. (1992). Rock magnetism of late Neogene and Pleistocene deep-sea sediments: relationship to sediment source, diagenetic processes, and sediment lithology. *Journal of Geophysical Research*, *97*(B4), 4361–4375. https://doi.org/10.1029/91JB03068

Chang, L., Harrison, R. J., & Berndt, T. A. (2019). Micromagnetic simulation of magnetofossils with realistic size and shape distributions: Linking magnetic proxies with nanoscale observations and implications for magnetofossil identification. *Earth and Planetary Science Letters*, *527*. https://doi.org/10.1016/j.epsl.2019.115790

Chang, L., Heslop, D., Roberts, A. P., Rey, D., & Mohamed, K. J. (2016). Discrimination of biogenic and detrital magnetite through a double Verwey transition temperature. *Journal of Geophysical Research: Solid Earth*, *121*(1), 3–14. https://doi.org/10.1002/2015JB012485

Chang, L., Hong, H., Bai, F., Wang, S., Pei, Z., Paterson, G. A., Heslop, D., Roberts, A. P., Huang, B., Tauxe, L., & Muxworthy, A. R. (2021). Detrital remanent magnetization of single-crystal silicates with magnetic inclusions: Constraints from deposition experiments. *Geophysical Journal International*, *224*(3), 2001–2015. https://doi.org/10.1093/gji/ggaa559

Chang, L., Roberts, A. P., Heslop, D., Hayashida, A., Li, J., Zhao, X., Tian, W., & Huang, Q. (2016). Widespread occurrence of silicate-hosted magnetic mineral inclusions in marine sediments and their contribution to paleomagnetic recording. *Journal of Geophysical Research: Solid Earth*, *121*(12), 8415–8431. https://doi.org/10.1002/2016JB013109

Chang, L., Winklhofer, M., Roberts, A. P., Heslop, D., Florindo, F., Dekkers, M. J., Krijgsman, W., Kodama, K., & Yamamoto, Y. (2013). Low-temperature magnetic properties of pelagic carbonates: Oxidation of biogenic magnetite and identification of magnetosome chains. *Journal of Geophysical Research: Solid Earth*, *118*(12), 6049–6065. https://doi.org/10.1002/2013JB010381

Channell, J. E. T., Singer, B. S., & Jicha, B. R. (2020). Timing of Quaternary geomagnetic reversals and excursions in volcanic and sedimentary archives. *Quaternary Science Reviews*, *228*, 106114. https://doi.org/10.1016/J.QUASCIREV.2019.106114

Channell, J. E. T., Xuan, C., & Hodell, D. A. (2009). Stacking paleointensity and oxygen isotope data for the last 1.5 Myr (PISO-1500). *Earth and Planetary Science Letters*, *283*(1–4), 14–23. https://doi.org/10.1016/J.EPSL.2009.03.012

Chen, L., Heslop, D., Roberts, A. P., Chang, L., Zhao, X., McGregor, H. v., Marino, G., Rodriguez-Sanz, L., Rohling, E. J., & Pälike, H. (2017). Remanence acquisition efficiency in biogenic and detrital magnetite and recording of geomagnetic paleointensity. *Geochemistry, Geophysics, Geosystems*, *18*(4), 1435–1450. https://doi.org/10.1002/2016GC006753

Cisowski, S. (1981). Interacting vs. non-interacting single domain behavior in natural and synthetic samples. *Physics of the Earth and Planetary Interiors*, *26*(1–2), 56–62. https://doi.org/10.1016/0031-9201(81)90097-2

Clayton, R. N., Rex, R. W., Syers, J. K., & Jackson, M. L. (1972). Oxygen isotope abundance in quartz from Pacific pelagic sediments. *Journal of Geophysical Research*, *77*(21), 3907–3915. https://doi.org/10.1029/JC077i021p03907

Cui, Y., Verosub, K. L., & Roberts, A. P. (1994). *The effect of low-temperature oxidation on large multi-domain magnetite* (Vol. 21, Issue 9).

Dang, H., Wu, J., Xiong, Z., Qiao, P., Li, T., & Jian, Z. (2020). Orbital and sea-level changes regulate the iron-associated sediment supplies from Papua New Guinea to the equatorial Pacific. *Quaternary Science Reviews*, *239*. https://doi.org/10.1016/j.quascirev.2020.106361

Egli, R. (2004). Characterization of individual rock magnetic components by analysis of remanence curves. 2. Fundamental properties of coercivity distributions. *Physics and Chemistry of the Earth*, *29*(13-14 SPEC. ISS.), 851–867. https://doi.org/10.1016/j.pce.2004.04.001

Egli, R. (2013). VARIFORC: An optimized protocol for calculating non-regular first-order reversal curve (FORC) diagrams. *Global and Planetary Change*, *110*, 302–320. https://doi.org/10.1016/j.gloplacha.2013.08.003

Egli, R. (2021). Magnetic Characterization of Geologic Materials with First-Order Reversal Curves. In V. Franco & B. Dodrill (Eds.), *Magnetic Measurement Techniques for Materials Characterization* (pp. 455–604). Springer International Publishing. https://doi.org/10.1007/978-3-030-70443-8_17

Egli, R., Chen, A. P., Winklhofer, M., Kodama, K. P., & Horng, C.-S. (2010). Detection of noninteracting single domain particles using first-order reversal curve diagrams. *Geochemistry, Geophysics, Geosystems*, *11*(1), n/a-n/a. https://doi.org/10.1029/2009gc002916

Feinberg, J. M., Harrison, R. J., Kasama, T., Dunin-Borkowski, R. E., Scott, G. R., & Renne, P. R. (2006). Effects of internal mineral structures on the magnetic remanence of silicate-hosted titanomagnetite inclusions: An electron holography study. *Journal of Geophysical Research: Solid Earth*, *111*(12). https://doi.org/10.1029/2006JB004498

Flanders, P. J. (1988). An alternating-gradient magnetometer (invited). *Journal of Applied Physics*, *63*(8), 3940–3945. https://doi.org/10.1063/1.340582

Harrison, R. J., & Feinberg, J. M. (2008). FORCinel: An improved algorithm for calculating first-order reversal curve distributions using locally weighted regression smoothing. *Geochemistry, Geophysics, Geosystems*, *9*(5). https://doi.org/10.1029/2008GC001987

Hofmann, D. I., & Fabian, K. (2009). Correcting relative paleointensity records for variations in sediment composition: Results from a South Atlantic stratigraphic network. *Earth and Planetary Science Letters*, *284*(1–2), 34–43. https://doi.org/10.1016/j.epsl.2009.03.043

Hong, H., Chang, L., Hayashida, A., Roberts, A. P., Heslop, D., Paterson, G. A., Kodama, K., & Tauxe, L. (2019). Paleomagnetic Recording Efficiency of Sedimentary Magnetic Mineral Inclusions: Implications for Relative Paleointensity Determinations. *Journal of Geophysical Research: Solid Earth*, *124*(7), 6267–6279. https://doi.org/10.1029/2018JB016859

Inoue, K., Yamazaki, T., & Usui, Y. (2021). Influence of Magnetofossils on Paleointensity Estimations Inferred From Principal Component Analyses of First-Order Reversal Curve Diagrams for Sediments From the Western Equatorial Pacific. *Geochemistry, Geophysics, Geosystems*, *22*(10). https://doi.org/10.1029/2021GC010081

Johnson, C. L., & Constable, C. G. (1997). The time-averaged geomagnetic field: global and regional biases for 0–5 Ma. *Geophysical Journal International*, *131*(3), 643–666. https://doi.org/10.1111/j.1365-246X.1997.tb06604.x

Johnson, E. A., Murphy, T., & Torreson, O. W. (1948). *Prehistory of the Earth's Magnetic Field*.

King, J., Banerjee, S. K., Marvin, J., & Özdemir, Ö. (1982). A comparison of different magnetic methods for determining the relative grain size of magnetite in natural materials: Some results from lake sediments. *Earth and Planetary Science Letters*, *59*(2), 404–419. https://doi.org/10.1016/0012-821X(82)90142-X

King, J. W., Banerjee, S. K., & Marvin, J. (1983). A new rock- magnetic approach to selecting sediments for geomagnetic paleointensity studies: application to paleointensity for the last 4000 years. *Journal of Geophysical Research*, *88*(B7), 5911–5921. https://doi.org/10.1029/JB088iB07p05911

Kirschvink, J. L. (1980). The least-squares line and plane and the analysis of palaeomagnetic data. *Geophysical Journal International*, *62*(3), 699–718. https://doi.org/10.1111/j.1365-246X.1980.tb02601.x

Kirschvink, J. L. (1982). Paleomagnetic evidence for fossil biogenic magnetite in western Crete. *Earth and Planetary Science Letters*, *59*(2), 388–392. https://doi.org/10.1016/0012-821X(82)90140-6

Kopp, R. E., & Kirschvink, J. L. (2008). The identification and biogeochemical interpretation of fossil magnetotactic bacteria. *Earth-Science Reviews*, *86*(1–4), 42–61. https://doi.org/10.1016/J.EARSCIREV.2007.08.001

Lascu, I., & Plank, C. (2013). A new dimension to sediment magnetism: Charting the spatial variability of magnetic properties across lake basins. *Global and Planetary Change*, *110*, 340–349. https://doi.org/10.1016/J.GLOPLACHA.2013.03.013

Levi, S., & Banerjee, S. K. (1976). On the possibility of obtaining relative paleointensities from lake sediments. In *Earth and Planetary Science Letters* (Vol. 29).

Li, J., Ge, K., Pan, Y., Williams, W., Liu, Q., & Qin, H. (2013). A strong angular dependence of magnetic properties of magnetosome chains: Implications for rock magnetism and paleomagnetism. *Geochemistry, Geophysics, Geosystems*, *14*(10), 3887–3907. https://doi.org/10.1002/ggge.20228

Li, J., Menguy, N., Roberts, A. P., Gu, L., Leroy, E., Bourgon, J., Yang, X., Zhao, X., Liu, P., Changela, H. G., & Pan, Y. (2020). Bullet-Shaped Magnetite Biomineralization Within a Magnetotactic Deltaproteobacterium: Implications for Magnetofossil Identification. *Journal of Geophysical Research: Biogeosciences*, *125*(7). https://doi.org/10.1029/2020JG005680

Li, J., Pan, Y., Chen, G., Liu, Q., Tian, L., & Lin, W. (2009). Magnetite magnetosome and fragmental chain formation of Magnetospirillum magneticum AMB-1: Transmission electron microscopy and magnetic observations. *Geophysical Journal International*, *177*(1), 33–42. https://doi.org/10.1111/j.1365-246X.2009.04043.x

Li, J., Wu, W., Liu, Q., & Pan, Y. (2012). Magnetic anisotropy, magnetostatic interactions and identification of magnetofossils. *Geochemistry, Geophysics, Geosystems*, *13*(10). https://doi.org/10.1029/2012GC004384

Lisiecki, L. E., & Raymo, M. E. (2005). A Pliocene-Pleistocene stack of 57 globally distributed benthic δ 18O records. *Paleoceanography*, *20*(1), 1–17. https://doi.org/10.1029/2004PA001071

Liu, J., Zhu, R., Roberts, A. P., Li, S., & Chang, J.-H. (2004). High-resolution analysis of early diagenetic effects on magnetic minerals in post-middle-Holocene continental shelf sediments from the Korea Strait. *Journal of Geophysical Research: Solid Earth*, *109*(B3). https://doi.org/https://doi.org/10.1029/2003JB002813

Mitra, R., & Tauxe, L. (2009). Full vector model for magnetization in sediments. *Earth and Planetary Science Letters*, *286*(3–4), 535–545. https://doi.org/10.1016/J.EPSL.2009.07.019

Nagata, T. (1961). *Rock Magnetism* (Vol. 350). Maruzen Company Ltd.

O'Reilly, W. (1984). *Rock and mineral magnetism*. Glasgow : Blackie. http://lib.ugent.be/catalog/rug01:000714155

Ouyang, T., Heslop, D., Roberts, A. P., Tian, C., Zhu, Z., Qiu, Y., & Peng, X. (2014). Variable remanence acquisition efficiency in sediments containing biogenic and detrital magnetites: Implications for relative paleointensity signal recording. *Geochemistry, Geophysics, Geosystems*, *15*(7), 2780–2796. https://doi.org/10.1002/2014GC005301

Özdemir, Ö., & Dunlop, D. J. (2010). Hallmarks of maghemitization in low-temperature remanence cycling of partially oxidized magnetite nanoparticles. *Journal of Geophysical Research*, *115*(B2). https://doi.org/10.1029/2009jb006756

Pan, Y., Petersen, N., Winklhofer, M., Davila, A. F., Liu, Q., Frederichs, T., Hanzlik, M., & Zhu, R. (2005). Rock magnetic properties of uncultured magnetotactic bacteria. *Earth and Planetary Science Letters*, *237*(3–4), 311–325. https://doi.org/10.1016/j.epsl.2005.06.029

Paterson, G. A., Wang, Y., & Pan, Y. (2013). The fidelity of paleomagnetic records carried by magnetosome chains. *Earth and Planetary Science Letters*, *383*, 82–91. https://doi.org/10.1016/j.epsl.2013.09.031

Pike, C. R. (2003). First-order reversal-curve diagrams and reversible magnetization. *Physical Review B*, *68*(10), 104424. https://doi.org/10.1103/PhysRevB.68.104424

Pike, C. R., Roberts, A. P., & Verosub, K. L. (1999). Characterizing interactions in fine magnetic particle systems using first order reversal curves. *Journal of Applied Physics*, *85*(9), 6660–6667. https://doi.org/10.1063/1.370176

Pike, C. R., Roberts, A. P., & Verosub, K. L. (2001). First order reversal curve diagrams and thermal relaxation effects in magnetic particles. *Geophysical Journal International*, *145*(3), 721–730. https://doi.org/10.1046/j.0956-540x.2001.01419.x

Rea, D. K. (1994). The paleoclimatic record provided by eolian deposition in the deep sea: The geologic history of wind. *Reviews of Geophysics*, *32*(2), 159–195. https://doi.org/https://doi.org/10.1029/93RG03257

Roberts, A. P., Chang, L., Heslop, D., Florindo, F., & Larrasoaa, J. C. (2012). Searching for single domain magnetite in the "pseudo-single- domain" sedimentary haystack: Implications of biogenic magnetite preservation for sediment magnetism and relative paleointensity determinations. *Journal of Geophysical Research: Solid Earth*, *117*(8). https://doi.org/10.1029/2012JB009412

Roberts, A. P., Heslop, D., Zhao, X., & Pike, C. R. (2014). Understanding fine magnetic particle systems through use of first-order reversal curve diagrams. In *Reviews of Geophysics* (Vol. 52, Issue 4, pp. 557–602). Blackwell Publishing Ltd. https://doi.org/10.1002/2014RG000462

Roberts, A. P., Pike, C. R., & Verosub, K. L. (2000). First-order reversal curve diagrams: A new tool for characterizing the magnetic properties of natural samples. *Journal of Geophysical Research: Solid Earth*, *105*(B12), 28461–28475. https://doi.org/10.1029/2000jb900326

Roberts, A. P., Tauxe, L., & Heslop, D. (2013). Magnetic paleointensity stratigraphy and high-resolution Quaternary geochronology: Successes and future challenges. In *Quaternary Science Reviews* (Vol. 61, pp. 1–16). https://doi.org/10.1016/j.quascirev.2012.10.036

Sakuramoto, Y., Yamazaki, T., Kimoto, K., Miyairi, Y., Kuroda, J., Yokoyama, Y., & Matsuzaki, H. (2017). A Geomagnetic Paleointensity Record of 0.6 to 3.2 Ma From Sediments in the Western Equatorial Pacific and Remanent Magnetization Lock-In Depth. *Journal of Geophysical Research: Solid Earth*, *122*(10), 7525–7543. https://doi.org/10.1002/2017JB014450

Singer, B. S. (2014). A Quaternary geomagnetic instability time scale. *Quaternary Geochronology*, *21*(1), 29–52. https://doi.org/10.1016/J.QUAGEO.2013.10.003

Stevens, R. L. (1991). Grain-size distribution of quartz and feldspar extracts and implications for flocculation processes. *Geo-Marine Letters*, *11*(3), 162–165. https://doi.org/10.1007/BF02431004

Stoner, E. C., & Wohlfarth, E. P. (1948). A mechanism of magnetic hysteresis in heterogeneous alloys. *Philosophical Transactions of the Royal Society of London. Series A, Mathematical and Physical Sciences*, *240*(826), 599–642. https://doi.org/10.1098/rsta.1948.0007

Suganuma, Y., Haneda, Y., Kameo, K., Kubota, Y., Hayashi, H., Itaki, T., Okuda, M., Head, M. J., Sugaya, M., Nakazato, H., Igarashi, A., Shikoku, K., Hongo, M., Watanabe, M., Satoguchi, Y., Takeshita, Y., Nishida, N., Izumi, K., Kawamura, K., … Okada, M. (2018). Paleoclimatic and paleoceanographic records through Marine Isotope Stage 19 at the Chiba composite section, central Japan: A key reference for the Early–Middle Pleistocene Subseries boundary. *Quaternary Science Reviews*, *191*, 406–430. https://doi.org/10.1016/J.QUASCIREV.2018.04.022

Sugiura, N. (1979). ARM, TRM and magnetic interactions: Concentration dependence. *Earth and Planetary Science Letters*, *42*(3), 451–455. https://doi.org/10.1016/0012-821X(79)90054-2

Syers, J. K., Chapman, S. L., Jackson, M. L., Rex, R. W., & Clayton, R. N. (1968). Quartz isolation from rocks, sediments and soils for determination of oxygen isotopes composition. *Geochimica et Cosmochimica Acta*, *32*(9), 1022–1025. https://doi.org/10.1016/0016-7037(68)90067-7

Tauxe, L. (1993). Sedimentary records of relative paleointensity of the geomagnetic field: Theory and practice. *Reviews of Geophysics*, *31*(3), 319–354. https://doi.org/https://doi.org/10.1029/93RG01771

Tauxe, L., Pick, T., & Kok, Y. S. (1995). *Relative paleointensity in sediments: a pseudo-Thellier approach* (Vol. 22, Issue 21). https://doi.org/10.1029/95GL03166

Tauxe, L., Steindorf, J. L., & Harris, A. (2006). Depositional remanent magnetization: Toward an improved theoretical and experimental foundation. *Earth and Planetary Science Letters*, *244*(3–4), 515–529. https://doi.org/10.1016/J.EPSL.2006.02.003

Tauxe, L., & Yamazaki, T. (2015). Paleointensities. In *Treatise on Geophysics: Second Edition* (Vol. 5, pp. 461–509). Elsevier Inc. https://doi.org/10.1016/B978-0-444-53802-4.00107-X

Usui, Y., Shimono, T., & Yamazaki, T. (2018). Rock magnetism of quartz and feldspars chemically separated from pelagic red clay: a new approach to provenance study. *Earth, Planets and Space*, *70*(1). https://doi.org/10.1186/s40623-018-0918-1

Usui, Y., & Yamazaki, T. (2021). Non-Chained, Non-Interacting, Stable Single-Domain Magnetite Octahedra in Deep-Sea Red Clay: A New Type of Magnetofossil? *Geochemistry, Geophysics, Geosystems*, *22*(7). https://doi.org/10.1029/2021GC009770

Usui, Y., Yamazaki, T., & Saitoh, M. (2017). Changing Abundance of Magnetofossil Morphologies in Pelagic Red Clay Around Minamitorishima, Western North Pacific. *Geochemistry, Geophysics, Geosystems*, *18*(12), 4558–4572. https://doi.org/https://doi.org/10.1002/2017GC007127

Valencia, M.]. (1973). Calcium Carbonate and Gross-Size Analysis of Surface Sediments, Western Equatorial Pacific I. In *Pacific Science* (Vol. 27, Issue 3).

van Velzen, A. J., & Zijderveld, J. D. A. (1995). Effects of weathering on single-domain magnetite in Early Pliocene marine marls. *Geophysical Journal International*, *121*(1), 267–278. https://doi.org/10.1111/j.1365-246X.1995.tb03526.x

Verwey, E. J. W. (1939). Electronic Conduction of Magnetite (Fe3O4) and its Transition Point at Low Temperatures. *Nature*, *144*(3642), 327–328. https://doi.org/10.1038/144327b0

Winckler, G., Anderson, R. F., Jaccard, S. L., & Marcantonio, F. (2016). Ocean dynamics, not dust, have controlled equatorial Pacific productivity over the past 500,000 years. *Proceedings of the National Academy of Sciences of the United States of America*, *113*(22), 6119–6124. https://doi.org/10.1073/pnas.1600616113

Wu, J., Liu, Z., & Zhou, C. (2013). Provenance and supply of Fe-enriched terrigenous sediments in the western equatorial Pacific and their relation to precipitation variations during the late Quaternary. *Global and Planetary Change*, *108*, 56–71. https://doi.org/10.1016/j.gloplacha.2013.06.002

Yamazaki, T. (2008). Magnetostatic interactions in deep-sea sediments inferred from first-order reversal curve diagrams: Implications for relative paleointensity normalization. *Geochemistry, Geophysics, Geosystems*, *9*(2). https://doi.org/10.1029/2007GC001797

Yamazaki, T. (2009). Environmental magnetism of Pleistocene sediments in the North Pacific and Ontong-Java Plateau: Temporal variations of detrital and biogenic components. *Geochemistry, Geophysics, Geosystems*, *10*(7). https://doi.org/10.1029/2009GC002413

Yamazaki, T. (2012). Paleoposition of the Intertropical Convergence Zone in the eastern Pacific inferred from glacial-interglacial changes in terrigenous and biogenic magnetic mineral fractions. *Geology*, *40*(2), 151–154. https://doi.org/10.1130/G32646.1

Yamazaki, T. (2020). Reductive dissolution of biogenic magnetite. *Earth, Planets and Space*, *72*(1). https://doi.org/10.1186/s40623-020-01290-3

Yamazaki, T., Abdeldayem, A. L., & Ikehara, K. (2003). Rock-magnetic changes with reduction diagenesis in Japan Sea sediments and preservation of geomagnetic secular variation in inclination during the last 30,000 years. *Earth, Planets and Space*, *55*(6), 327–340. https://doi.org/10.1186/BF03351766

Yamazaki, T., Fu, W., Shimono, T., & Usui, Y. (2020). Unmixing biogenic and terrigenous magnetic mineral components in red clay of the Pacific Ocean using principal component analyses of first-order reversal curve diagrams and paleoenvironmental implications. Earth, Planets and Space, 72(1), 120. https://doi.org/10.1186/s40623-020-01248-5

Yamazaki, T., & Ikehara, M. (2012). Origin of magnetic mineral concentration variation in the Southern Ocean. *Paleoceanography*, *27*(2). https://doi.org/10.1029/2011PA002271

Yamazaki, T., Kanamatsu, T., Mizuno, S., Hokanishi, N., & Gaffar, E. Z. (2008). Geomagnetic field variations during the last 400 kyr in the western equatorial Pacific: Paleointensity-inclination correlation revisited. *Geophysical Research Letters*, *35*(20). https://doi.org/10.1029/2008GL035373

Yamazaki, T., & Shimono, T. (2013). Abundant bacterial magnetite occurrence in oxic red clay. *Geology*, *41*(11), 1191–1194. https://doi.org/10.1130/G34782.1

Yamazaki, T., & Solheid, P. (2011). Maghemite-to-magnetite reduction across the Fe-redox boundary in a sediment core from the Ontong-Java Plateau: Influence on relative palaeointensity estimation and environmental magnetic application. *Geophysical Journal International*, *185*(3), 1243–1254. https://doi.org/10.1111/j.1365-246X.2011.05021.x

Yamazaki, T., & Yamamoto, Y. (2018). Relative Paleointensity and Inclination Anomaly Over the Last 8 Myr Obtained From the Integrated Ocean Drilling Program Site U1335 Sediments in the Eastern Equatorial Pacific. *Journal of Geophysical Research: Solid Earth*, *123*(9), 7305–7320. https://doi.org/10.1029/2018JB016209

Yamazaki, T., Yamamoto, Y., Acton, G., Guidry, E. P., Richter, C., Yamazaki, T., Yamamoto, Y., Acton, G., Guidry, E. P., & Richter, C. (2013). Rock-magnetic artifacts on long-term relative paleointensity variations in sediments. *Geochem. Geophys. Geosyst*, *14*, 29–43. https://doi.org/10.1029/2012GC004546

Zhang, Q., Liu, Q., Li, J., & Sun, Y. (2018). An Integrated Study of the Eolian Dust in Pelagic Sediments From the North Pacific Ocean Based on Environmental Magnetism, Transmission Electron Microscopy, and Diffuse Reflectance Spectroscopy. *Journal of Geophysical Research: Solid Earth*, *123*(5), 3358–3376. https://doi.org/10.1002/2017JB014951